OXFORD

Forearc Peridotites from Tonga Record Heterogeneous Oxidation of the Mantle following Subduction Initiation

Suzanne K. Birner[1,2]*, Jessica M. Warren[3], Elizabeth Cottrell[2], Fred A. Davis[4], Katherine A. Kelley[5] and Trevor J. Falloon[6]

[1]Department of Geological Sciences, Stanford University, 450 Serra Mall, Building 320, Stanford, CA 94305, USA; [2]National Museum of Natural History, Smithsonian Institution, Washington, DC 20560, USA; [3]Department of Geological Sciences, University of Delaware, Penny Hall, Newark, DE 19716, USA; [4]Department of Earth and Environmental Sciences, University of Minnesota Duluth, 229 Heller Hall, 1114 Kirby Drive, Duluth, MN 55812, USA; [5]Graduate School of Oceanography, University of Rhode Island, Narragansett, RI 02882, USA; [6]School of Physical Sciences, Discipline of Earth Sciences, University of Tasmania, Hobart, TAS 7001, Australia

*Corresponding author. Telephone: 1-847-830-8341. E-mail: skbirner@stanford.edu

ABSTRACT

The elevated oxygen fugacity recorded by subduction-related lavas and peridotites, relative to their mid-ocean ridge counterparts, fundamentally influences the petrogenesis of arc magmas. However, the timing, process, and spatial extent of oxidizing mass transfer at subduction zones remain unknown. Forearc peridotites, which are sometimes exposed on the trench wall of the overriding plate, record chemical fingerprints of the melting and melt–rock interaction processes that occur during and following subduction initiation, and thus provide insight into the spatial and temporal evolution of this oxidized signature. In this study, we present new major element, trace element, and oxygen fugacity data for a suite of forearc peridotites recovered from the Tonga Trench, in addition to a new assessment of literature data for previously studied forearc peridotites. For Tonga samples and literature data for forearc, ridge, and subduction-zone peridotites, we calculate oxygen fugacity (f_{O_2}) using an updated method. In contrast to previous studies, we find that spinel Cr#, a proxy for extent of melt extraction, does not correlate with oxygen fugacity, such that many forearc peridotites with high spinel Cr# do not record oxygen fugacity higher than the mid-ocean ridge peridotite array. Combining these observations with trace element modeling, we conclude that forearc peridotites are less pervasively influenced by oxidation owing to subduction processes than previously reported. The oxygen fugacity recorded by Tonga forearc peridotites is heterogeneous between dredges and homogeneous within dredges. To explore these variations, we grouped the dredges into two categories. Group I peridotites have high spinel Cr#, extremely depleted trace element compositions and oxygen fugacity values consistent with the mid-ocean ridge peridotite array. We interpret these to be the residues of large degrees of fractional melting, with little influence from arc-like melts or fluids, formed during the first stages of subduction initiation. Group II peridotites have lower spinel Cr#, enriched light rare earth elements, and oxygen fugacity elevated by ≥ 1 log unit above the mid-ocean peridotite array. We interpret these peridotites to be the residues of flux melting, initiated once corner flow is established in the young subduction zone. We conclude that the forearc mantle is not pervasively oxidized relative to mid-ocean ridge mantle, and that the asthenospheric mantle in the proto-subduction zone region is not oxidized prior to subduction initiation. As the oxidized signature in Group II peridotites accompanies geochemical evidence of interaction with subduction-related fluids and melts, this suggests

that the sub-arc mantle is oxidized concurrently with addition of subduction fluids to the mantle wedge.

Key words: forearc; oxygen fugacity; subduction; Tonga; upper mantle

INTRODUCTION

Subduction zones are major loci of mass transfer between the Earth's surface and interior, recycling oceanic lithosphere and sediments while generating arc volcanism at the surface. Forearc sequences may record the evolution of mass transfer at arcs, from initiation through to maturity (Reagan *et al.*, 2010, 2015; Ishizuka *et al.*, 2011; Brounce *et al.*, 2015). Within these sequences, forearc peridotites—tectonically exposed pieces of lithospheric mantle originating from the overriding plate—provide a major avenue for investigating mass transfer in arc settings (Deschamps *et al.*, 2013), including mass transfer that may result in oxidation. As a result of seafloor alteration, the subducting plate may return significant quantities of oxidized rock to the subsurface (e.g. Evans, 2012), where it dehydrates to generate arc melts in the mantle wedge via flux melting (e.g. Grove *et al.*, 2006). Mass transfer that results in variations in mantle oxygen fugacity (f_{O_2}) in turn influences phase stability, liquid lines of descent, volatile speciation and the position of the mantle solidus (e.g. Wood *et al.*, 1990; Stagno *et al.*, 2013; Gaillard *et al.*, 2015). Because forearc peridotite mineral assemblages can record oxygen fugacity, they may provide invaluable information about the timing, process, and spatial extent of oxidative mass transfer at subduction zones.

Studies of the oxygen fugacity of subduction-zone lithologies have shown that both volcanic rocks and peridotites from arcs are typically more oxidized than their ridge counterparts (e.g. Wood *et al.*, 1990; Carmichael, 1991). Based on analyses of erupted lavas, the oxygen fugacity of the mid-ocean ridge basalt (MORB) source mantle is at or just above the quartz–fayalite–magnetite (QFM) buffer (Bézos & Humler, 2005; Cottrell & Kelley, 2011), whereas the source of arc lavas may be more than an order of magnitude more oxidized (e.g. Carmichael, 1991; Kelley & Cottrell, 2009; Brounce *et al.*, 2014). Similarly, studies of mid-ocean ridge peridotites imply that the MORB source oxygen fugacity is below QFM (Bryndzia & Wood, 1990), whereas subduction-related peridotite xenoliths record oxygen fugacities above QFM + 1 (Wood & Virgo, 1989; Wood *et al.*, 1990; Parkinson & Arculus, 1999; Parkinson *et al.*, 2003).

Although it is generally accepted that oxidized material enters subduction zones via the down-going slab and oxidized lavas subsequently emerge from arc volcanoes, few demonstrations of a direct link exist (e.g. Kelley & Cottrell, 2009; Brounce *et al.*, 2014). Very little is known about the mass transfer processes and pathways that occur within the mantle wedge above a subducting slab. Dehydration of the slab produces aqueous fluids that percolate through the mantle wedge and induce flux melting (e.g. Grove *et al.*, 2006); however, the exact composition and redox state of these fluids are not well constrained (e.g. Gaillard *et al.*, 2015). Even less well-constrained are the spatial scales and extents to which fluid infiltration alters and/or oxidizes the mantle wedge. Because of this uncertainty, some studies (e.g. Lee *et al.*, 2005, 2010; Mallmann & O'Neill, 2009) have advanced the hypothesis that oxidation in arc lavas does not relate to oxidation of the mantle source, but is instead due to late-stage processes such as differentiation and degassing. According to the hypothesis of Lee *et al.* (2005), subduction xenoliths are also not representative of mantle wedge material, but are instead pieces of lithospheric mantle that have been altered by repeated interaction with percolating melts or fluids. Because of the intrinsic uncertainties in interpreting source conditions from arc volcanic rocks and xenoliths, analysis of forearc peridotites provides a useful additional perspective on the redox state of arc mantle.

Non-accretionary intra-oceanic arcs often expose forearc peridotites, either within the trench on the wall of the overriding plate or exhumed in serpentine seamounts (e.g. Fryer *et al.*, 1985; Parkinson & Pearce, 1998; Pearce *et al.*, 2000). Previous studies investigating the chemistry and oxygen fugacity of forearc mantle have documented heterogeneous oxygen fugacity, extending from values similar to those of ridge peridotites up to values similar to those of arc xenoliths, and degrees of melt extraction extending to values greater than those at ridges (e.g. Parkinson & Pearce, 1998; Pearce *et al.*, 2000; Dare *et al.*, 2009). These signatures are interpreted as recording the redox effects of a variety of subduction-related melting and melt–rock reaction events.

In this study, we investigate the chemical signatures and oxygen fugacity recorded by forearc peridotites from the Tonga Trench to assess the role of subduction-zone melts and fluids in oxidizing the mantle. We find that the Tonga forearc mantle is heterogeneous, in terms of both recorded oxygen fugacity and major and trace element compositions. We additionally recalculate forearc peridotite data previously published in the literature using updated methods. We then assess the relative influence of flux melting and dry, near-fractional melting on forearc chemistry, both for our Tonga samples and for the literature data, and conclude that oxidation is not a pervasive feature of the forearc mantle. Instead, oxidation in forearc peridotites accompanies geochemical signatures indicative of interaction with arc fluids and melts.

SETTING

The Tonga Trench extends 1500 km along the northern segment of the Tonga–Kermadec arc system, a convergent margin in the SW Pacific where the Pacific Plate subducts under the Australian Plate (Fig. 1). The trench records the fastest plate convergence velocity on the planet, with the Tonga arc moving up to 240 mm a^{-1} in a Pacific-fixed reference frame (Bevis *et al.*, 1995), primarily owing to rapid rollback of the subducting slab. Behind the Tonga arc, the Lau back-arc basin is also spreading rapidly, at a rate variable with latitude—from 160 mm a^{-1} in the north to 60 mm a^{-1} in the south (Bevis *et al.*, 1995; Taylor *et al.*, 1996).

Subduction at the Tonga Trench began at *c.* 52 Ma (e.g. Meffre *et al.*, 2012), which is roughly concurrent with estimates for the age of subduction initiation at the more northerly Izu–Bonin–Mariana arc (e.g. Tani *et al.*, 2009; Ishizuka *et al.*, 2011) and just prior to the age of the bend in the Hawaii–Emperor Seamount Chain (Sharp & Clague, 2006). The Tonga forearc exposes a range of intrusive and extrusive lithologies, ranging from peridotites, gabbros and plagiogranites to MORB-like tholeiites, back-arc basin-like tholeiites, arc tholeiites, boninites, and rhyolites (Fisher & Engel, 1969; Bloomer & Fisher, 1987; Meffre *et al.*, 2012). This range of lithologies is similar to those reported for the Mariana forearc, which has been extensively mapped and exposes ultramafic lithologies overlain by gabbros, basalts, boninites, and other volcanic rocks interpreted to be associated with subduction initiation (e.g. Ohara *et al.*, 2008; Reagan *et al.*, 2010). The present-day Tonga arc lies on relatively young volcanic basement, 170–210 km from the trench axis, and defines the depleted end-member for intra-oceanic arc systems, with volcanic arc rocks showing variable evidence for sediment and fluid contributions (Plank & Langmuir, 1993; Turner *et al.*, 1997). At the northern terminus of the trench, the trench axis curves westward near the Samoan hotspot, resulting in slab window volcanism and production of young boninites and adakites (Falloon *et al.*, 2008; Resing *et al.*, 2011).

SAMPLES AND PETROGRAPHY

The lack of an accretionary wedge within the Tonga Trench results in tectonic exposure of lithospheric upper mantle on the trench wall of the overriding plate (Clift *et al.*, 1998). Forearc peridotites have been recovered in 14 dredges from along nearly 1000 km of the Tonga Trench, at depths ranging from 5·5 to 9·4 km below sea level (Fisher & Engel, 1969; Bloomer & Fisher, 1987; Bloomer *et al.*, 1996; Wright *et al.*, 2000). A subset of these samples is remarkably unaltered for seafloor peridotites (Birner *et al.*, 2016), as shown in Fig. 2. Values for loss on ignition (LOI) range from ∼0 to 20% [Supplementary Data (SD) Electronic Appendix 1; supplementary data are available for downloading at http://www.petrology.oxfordjournals.org] and correlate with the alteration score assigned from petrography (Fig. 3a). The large number of samples containing unaltered primary mantle minerals in some dredges allows intra-dredge systematics to be studied. Additionally, the collection of peridotites from multiple locations along the strike of the trench allows spatial comparison of geochemical properties along the trench axis.

Peridotites were dredged during the 1967 NOVA cruise (Fisher & Engel, 1969), the 1970 7TOW cruise (Bloomer & Fisher, 1987), and the 1996 Boomerang Leg 8 cruise (Bloomer *et al.*, 1996; Wright *et al.*, 2000). We initially analyzed the bulk-rock major and trace element composition of 26 peridotites from 13 dredges by X-ray fluorescence (XRF) and inductively coupled plasma mass spectrometry (ICP-MS) (SD Electronic Appendix 1). In this study, we focus on five dredges (BMRG08-98, BMRG08-106, BMRGG08-111, NOVA88, and 7TOW-57), based on the number of fresh, analyzable samples available. Dredge BMRG08-114 was excluded from further analysis, despite having abundant fresh material, because of the presence of plagioclase and ilmenite, suggesting late-stage melt impregnation. Table 1 summarizes each dredge and the analyses done.

Tonga peridotites are generally more refractory than the ridge peridotite array, with an average bulk-rock Al$_2$O$_3$ content of 0·7 ± 0·4 wt % (*n* = 26; SD Electronic
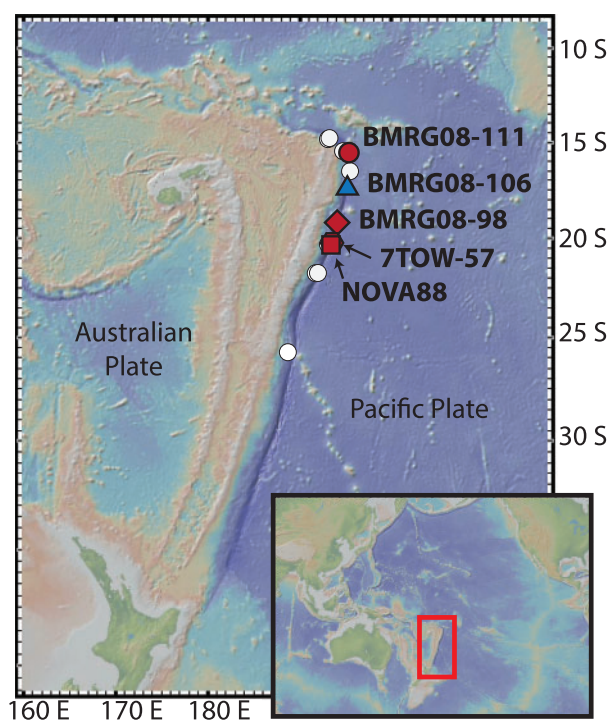
Fig. 1. Dredge locations for Tonga peridotite samples. Colored symbols represent dredge locations for peridotites analyzed in detail in this study: BMRG08-98, BMRG08-106, BMRG08-111, NOVA88, and 7TOW-57. White circles represent Boomerang08 dredge locations of peridotites not analyzed in detail in this study. Dredge locations are given in Table 1. The base map was created using GeoMapApp (www.geomapapp.org; Ryan *et al.*, 2009).
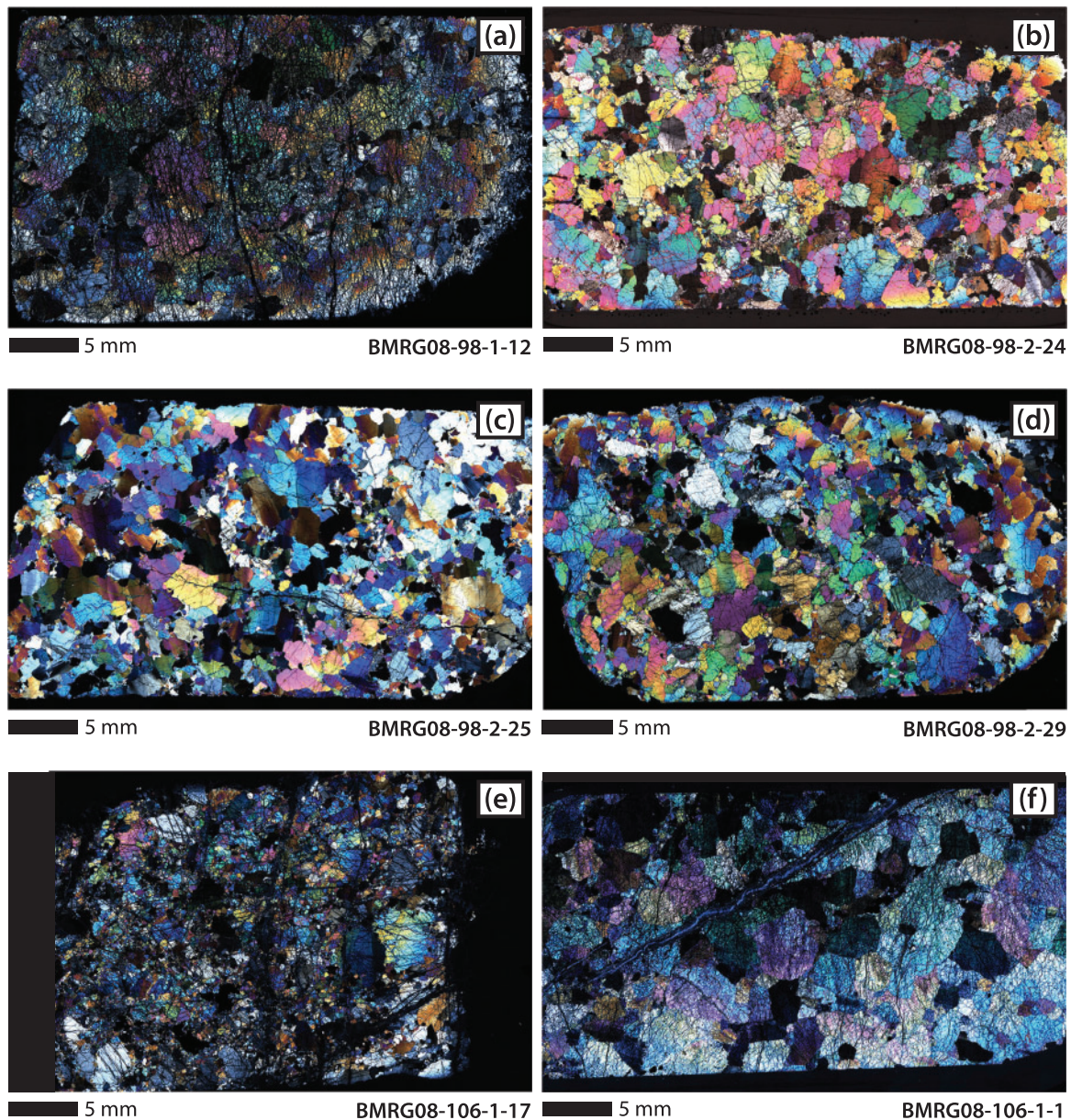
Fig. 2. Photomicrographs of representative Tonga peridotites from the focus dredges. (a) Sample BMRG08-98-1-12: harzburgite, alteration score = 3. (b) Sample BMRG08-98-2-24: harzburgite, alteration score = 1·5. (c) Sample BMRG08-98-2-25: harzburgite, alteration score = 1. (d) Sample BMRG08-98-2-29: harzburgite, alteration score = 1·5. (e) Sample BMRG08-106-1-17: harzburgite, alteration score = 2. (f) Sample BMRG08-106-1-1: dunite, alteration score = 2·5.

Appendix 1), compared with a ridge peridotite average of 1.6 ± 0.9 wt % ($n = 323$; Warren, 2016), as shown in Fig. 3b. Peridotites from the focus dredges are primarily highly refractory harzburgites (<2% clinopyroxene), with a few dunites (<10% total pyroxene) and only one confirmed lherzolite (>5% clinopyroxene; sample BMRG08-111-3-6). Mineral modes are plotted in Fig. 3c, based on point counts of representative samples reported in SD Electronic Appendix 2.

Texturally, the Tonga peridotites are protogranular to porphyroclastic, with no evidence in our focus dredges for high-strain deformation or large-scale melt addition (Fig. 2). Olivine and orthopyroxene grain sizes are relatively large (up to 5 mm in diameter), whereas clinopyroxene grains, when present, are small (<0·5 mm in diameter). Spinel grains range in size from ∼0·5 mm to ∼2 mm in diameter, and are intergrown with orthopyroxene in some cases, although symplectitic textures are not observed. Spinel grains have sharp boundaries and we did not observe sieve textures (e.g. Shaw & Dingwell, 2008) or compositional zonation in backscattered electron images. Pyroxenite and gabbro veins are also not observed, and no evidence of plagioclase or high-temperature amphibole was found in any sample from the five focus dredges.

The characteristics of dredges are as follows.

BMRG08-98. This dredge has the largest number of relatively unaltered samples. We analyzed 14 of the
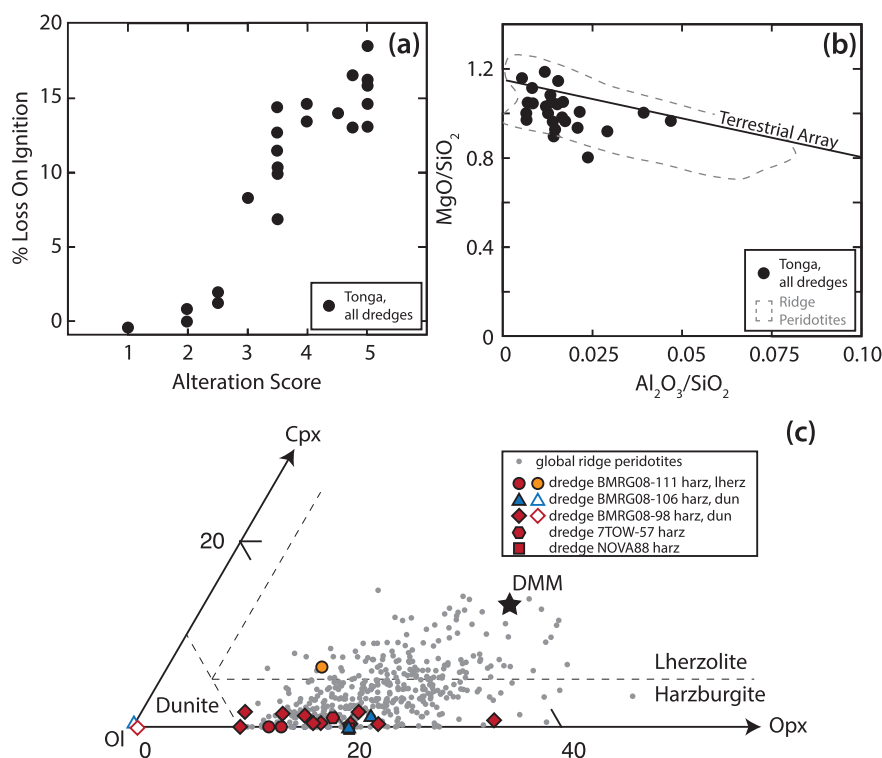
Fig. 3. (a) Per cent loss on ignition (LOI) vs alteration score for the Tonga peridotites. Alteration scores are taken from Birner *et al.* (2016), and LOI values are from this study. LOI is traditionally used as a proxy for degree of water addition, and thus serpentinization. The good correlation between LOI and qualitative alteration score suggests that both proxies can be used to determine the degree of alteration undergone by a peridotite. (b) Bulk MgO/SiO_2 vs bulk Al_2O_3/SiO_2. Continuous line is the Terrestrial Array of Jagoutz *et al.* (1979). Dashed field is the ridge peridotite array (Bodinier & Godard, 2014). The low Al_2O_3/SiO_2 ratios of the Tonga peridotites indicate that they are extremely refractory. (c) Modal data for a representative set of Tonga peridotites. The majority of samples are extremely refractory harzburgites, containing variable amounts of orthopyroxene and <2% clinopyroxene. Dredges BMRG08-98 and BMRG08-106 contain dunites, which have essentially no orthopyroxene or clinopyroxene. Dredge BMRG08-111 contains primarily extremely refractory harzburgites as well as one lherzolite, the only one identified in the five focus dredges.

Table 1: Tonga forearc dredges with peridotite as a dredged lithology

Cruise	Dredge	Lat.	Long.	Depth (m)	Alteration	Bulk-rock (XRF/ICP-MS)	Ol (major-EPMA)	Opx (major-EPMA)	Sp (major-EPMA)	Cpx (major-EPMA)	Cpx (trace-ICP-MS)	f_{O_2}	Group
BMRG08	114	−14·75	−173·36	5796	2–4·5	•							
BMRG08	113	−14·81	−173·40	4103	3·5–5	•							
BMRG08	112	−15·43	−172·67	4335	4·5–5	•							
BMRG08	**111**	**−15·50**	**−172·34**	**7425**	**2·5–4·5**	•	•	•	•		•	•	I
BMRG08	107	−16·52	−172·30	6337	4·5–5	•							
BMRG08	**106**	**−17·42**	**−172·41**	**7423**	**2–3·5**	•	•	•	•	•	•	•	II
BMRG08	**98**	**−19·25**	**−172·94**	**8194**	**1–4**	•	•	•	•	•	•	•	I
7TOW	**57**	**−20·25**	**−173·24**	**9270**	**2**	•	•	•	•		•	•	I
BMRG08	92	−20·34	−173·34	7133	3·5–4·5	•							
BMRG08	93	−20·37	−173·40	5564	3·5–4·5	•							
NOVA	**88**	**−20·38**	**−173·27**	**9400**	**1·5–3**	•	•	•	•		•	•	I
BMRG08	89	−21·84	−173·97	7246	5	•							
BMRG08	91	−21·86	−174·05	6303	5	•							
BMRG08	82	−25·86	−175·42	5467	3·5–5	•							

Types of analyses and calculations done for each dredge are summarized. Dredges in bold are focused on in detail in this study. Group numbers are as defined in the text.

48 samples identified as peridotite in the dredge log, as well as four new samples (BMRG08-98-2-23, -24, -25, -29) that were initially categorized as dredge BMRG08-98 miscellaneous samples and had not previously been identified as peridotite. Of these 18 samples, 15 are refractory harzburgites and three are dunites. Samples are remarkably unaltered by serpentinization, containing some of the freshest peridotites ever dredged from the seafloor [alteration scores = 1–4, where 1 corresponds to completely fresh and 5 to completely altered peridotite, as defined by Birner *et al.* (2016)].

BMRG08-106. We analyzed seven of the 27 samples identified as peridotite in the dredge log. Of these seven samples, three are refractory harzburgites and four are dunites. Samples are in general more altered by serpentinization than BMRG08-98 samples (alteration scores = 2–3·5).

BMRG08-111. We analyzed six of the 11 samples identified as peridotite in the dredge log. Of these, one is a lherzolite and five are refractory harzburgites. Samples are in general more altered by serpentinization than BMRG08-98 and -106 samples (alteration scores = 2·5–4·5).

NOVA88. We analyzed four samples from this dredge, for which a detailed dredge log is not available. Dredge 88 contained 20 kg of harzburgite with minor dunite, and samples range from fresh to serpentinized (Fisher & Engel, 1969; Bloomer & Fisher, 1987). All four of the samples analyzed in this study are relatively unaltered harzburgites (alteration scores = 1·5–3).

7TOW-57. We analyzed two samples from this dredge, for which a detailed dredge log is also not available. As reported by Bloomer & Fisher (1987), this dredge consists of harzburgite and minor dunite, the majority of which are fresh. Both of the samples analyzed in this study are relatively unaltered harzburgites (alteration score = 2).

METHODS

Major element analysis

Single grains of olivine, orthopyroxene, and spinel were analyzed at Stanford University and the Smithsonian Institution using electron microprobes equipped with five wavelength-dispersive spectrometers (WDS). The same analytical conditions and standards were used on both instruments in most cases, as summarized in SD Electronic Appendix 3. For spinel and olivine, we used a focused beam diameter of $\sim$1–2 μm. For spinel, we analyzed 3–5 grains per thin section, with three points per grain. For olivine, we analyzed 4–6 points per thin section. Seeking an average pyroxene composition, we used a defocused beam diameter of 10 μm, and averaged 7–15 analyses from transects perpendicular to exsolution lamellae. Clinopyroxene grains, which are frequently absent, were analyzed in samples for which trace elements were also obtained.

To calculate oxygen fugacity, accurate and precise estimates for the ferric iron content of spinel are necessary. To determine ferric iron content by microprobe, we used the method of Davis *et al.* (2017). Below we provide a brief summary.

We calculated the $Fe^{3+}/\Sigma Fe$ ratios of the spinels by normalizing spinel cation proportions to three total cations, initially treating all Fe as Fe^{2+}, and then adjusting the Fe^{3+}/Fe^{2+} ratio to balance the charge deficiency or excess to four oxygens per three cations (Stormer, 1983). We then applied a Cr#-based correction to these calculated $Fe^{3+}/\Sigma Fe$ ratios. At the beginning and end of each electron microprobe session, we measured eight calibration spinel standards with $Fe^{3+}/\Sigma Fe$ ratios previously characterized by Mössbauer spectroscopy (Wood & Virgo, 1989). After calculating $\Delta Fe^{3+}/\Sigma Fe^{\text{Möss–EPMA}}$ and Cr# for each calibration spinel measurement, we determined the slope and intercept of the best-fit line (Wood & Virgo, 1989):

$$\Delta Fe^{3+}/\Sigma Fe^{\text{Möss–EPMA}} = A * \text{Cr\#} + B. \tag{1}$$

We used equation (1) to correct the calculated $Fe^{3+}/\Sigma Fe$ ratios of spinel unknowns measured during that session, with the correction applied irrespective of whether $\Delta Fe^{3+}/\Sigma Fe^{\text{Möss–EPMA}}$ and Cr# were strongly correlated or not, the rationale for which has been described in detail by Davis *et al.* (2017).

After applying this correction, negative oxide weight per cents were corrected to zero and totals less than 98·0 or greater than 101·5 were discarded. For olivine and pyroxene, points with totals less than 98·5 or greater than 101·5 were discarded.

Trace element analysis

Trace element analyses were carried out for clinopyroxene, orthopyroxene, and a limited number of olivine grains at the University of Rhode Island using a UP-213 Nd-YAG laser ablation system coupled to a Thermo X-Series II quadrupole ICP-MS system, following methods modified from Kelley *et al.* (2003) and Lytle *et al.* (2012). Isotopes analyzed were ^{26}Mg, ^{45}Sc, ^{47}Ti, ^{51}V, ^{52}Cr, ^{55}Mn, ^{59}Co, ^{60}Ni, ^{65}Cu, ^{85}Rb, ^{88}Sr, ^{89}Y, ^{90}Zr, ^{93}Nb, ^{137}Ba, ^{139}La, ^{140}Ce, ^{141}Pr, ^{146}Nd, ^{147}Sm, ^{151}Eu, ^{159}Tb, ^{160}Gd, ^{163}Dy, ^{165}Ho, ^{166}Er, ^{169}Tm, ^{172}Yb, ^{175}Lu, ^{178}Hf, ^{181}Ta, ^{208}Pb, ^{232}Th, and ^{238}U. Spot sizes and drill rates varied by sample and were chosen to maximize signal intensity, given the low trace element abundances in these samples. Spot sizes ranged from 80 to 160 μm, with serpentinization and cracks as the limiting factors. Drill rate was limited by sample thickness; thicker samples ($\sim$60 μm) were ablated at a rate of 2 μm s^{-1} (10 Hz laser repeat rate), whereas thinner samples ($\sim$30 μm) were ablated at 1 μm s^{-1} (5 Hz), both at a laser fluence of 15·9 J cm^{-2} for a 60 μm reference spot. Background was measured for 30 s, followed by ablation of the sample for 60 s. Eight standards (BHVO-2G, BCR-2G, BIR-1G, GOR 132-G, StHls-G, T1-G, ML-3B-G, KL2-G), analyzed using the same analytical conditions and an 80 μm spot size, were used to construct calibration curves based on published values (Kelley *et al.*, 2003; Jochum *et al.*, 2006). The calibration standards were analyzed once at the beginning of each day and instrumental drift was assessed by periodic analysis of San Carlos olivine, which served as a secondary standard. Calibration curves were linear for all elements ($R^2 > 0.99$) and drift was negligible over the course of all analytical sessions.

To reduce the data, spectra were normalized to ^{26}Mg as the internal standard. We determined detection limits for each element in each sample by comparing the signal during on-peak data acquisition with the variation within the background signal, such that data were

excluded if they fell within two standard deviations of the average background signal. Data points were also excluded if the accumulated counting errors were greater than 50% of the counts.

Surface contamination by Pb was evident in the laser signal and each spectrum was individually screened to exclude regions of high Pb at the beginning of each analysis. However, concentrations of Pb reported here have a larger uncertainty than that for other elements owing to the possible inclusion of surface Pb throughout the ablation signal. Although we present Pb data in this work, our concerns about contamination leave its interpretation ambiguous, and we do not further discuss its implications in the context of our results.

Oxygen fugacity

The oxygen fugacity of peridotites can be calculated using phase equilibrium between olivine, orthopyroxene, and spinel:

$$6Fe_2SiO_4 + O_2 \iff 2Fe_3O_4 + 3Fe_2Si_2O_6.$$

$$\text{olivine} \qquad \text{spinel} \qquad \text{opx} \qquad (2)$$
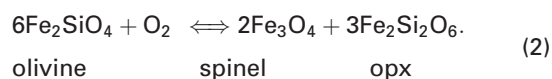
We calculated oxygen fugacity modified from the method of Mattioli & Wood (1988) and Wood & Virgo (1989), and the activity of magnetite in spinel using the MELTS Supplemental Calculator of Sack & Ghiorso (1991a, 1991b), as described by Davis *et al.* (2017). For the remainder of this discussion, the term 'f_{O2}' will be used to refer to oxygen fugacity relative to the solid buffer QFM of Frost (1991).

The calculation of f_{O2} depends on the pressure and temperature of equilibrium. For this study, we used the olivine–spinel thermometer of Li *et al.* (1995) and assumed a pressure of 0·6 GPa. We used this thermometer as olivine–spinel thermometry is based on the same elements and minerals (Fe and Mg content in olivine and spinel) that are used to calculate f_{O2}. This thermometer should give internal consistency with the oxybarometer as the two systems should have the same closure conditions. In Supplementary Data Section 1, we evaluate two pyroxene-based thermometers, which return higher temperatures owing to the higher closure temperatures for diffusion in pyroxene relative to spinel and olivine. We additionally provide justification for our use of the Li *et al.* (1995) thermometer over other spinel–olivine thermometers published in the literature.

As spinel peridotites lack a good barometer, we chose a pressure of 0·6 GPa to apply to all of our samples. Our goal in choosing this pressure was to maximize consistency with the temperature determined by the Li *et al.* (1995) thermometer, a relationship that depends on the thermal structure of the tectonic setting. Based on the model of Syracuse *et al.* (2010) for the thermal structure of the modern Tonga subduction zone, the model of Montési & Behn (2007) for the thermal structure of ultraslow-spreading mid-ocean ridges, and the experimental work of Borghini *et al.* (2010) on the stability of Cr-spinel as a function of pressure, we

estimate that 0·6 GPa is a reasonable pressure to apply to samples from both subduction zones and mid-ocean ridges. The relative f_{O2} of samples within a dredge is independent of the assumed pressure, as samples within a dredge follow the same exhumation path and thus equilibrate at the same pressure. Different dredges may reflect different pressures of equilibration; however, the effect of pressure on calculated f_{O2} is small (<0·5 log units per GPa), and thus uncertainty in pressure does not affect our overall conclusions.

We calculated error following the method of Davis *et al.* (2017) based on component analysis of the individual error associated with olivine, orthopyroxene, and spinel analyses, as well as P and T assumptions. Average total error for each point is ∼0·4 log units, with calculation of $Fe^{3+}/\Sigma Fe$ ratios contributing the largest uncertainty.

RECALCULATION OF LITERATURE f_{O2}

To maintain consistency with previously calculated peridotite f_{O2} data, we recalculated literature data according to our updated method (Davis *et al.*, 2017). Although this recalculation has a small effect on overall systematics for f_{O2} in most samples, some samples differ from their published value by up to a log unit. In particular, the activity model used for spinel has a large effect on calculated f_{O2}, as discussed below.

Studies implementing the Wood & Virgo (1989) oxybarometry method have used the Nell–Wood activity model (Nell & Wood, 1991) for calculating magnetite activity in spinel (e.g. Bryndzia & Wood, 1990; Parkinson & Pearce, 1998; Pearce *et al.*, 2000). We use the spinel model of Sack & Ghiorso (1991a, 1991b) in place of the Nell–Wood model, because previous studies (Herd, 2008; Davis *et al.*, 2017) have found that the Sack–Ghiorso model is a better fit to the Wood (1990) experimental data than the Nell–Wood model. In particular, Wood (1990) found that the Nell–Wood model underestimates calculated f_{O2} by 0·35 log units on average compared with experiments, whereas Herd (2008) showed that the Sack–Ghiorso model underestimates the f_{O2} of the same experiments only by 0·07 log units on average. Davis *et al.* (2017) further showed that by changing the way in which spinel endmembers are calculated, the underestimation of the Sack–Ghiorso model can be decreased to 0·03 log units. To maintain consistency, we have thus recalculated all literature data using the Sack–Ghiorso spinel model.

The recalculation of f_{O2} has a large effect on literature data at spinel Cr# >60 (Fig. 4). For example, the high-Cr# samples of Parkinson & Pearce (1998) are reduced by up to a log unit. In Fig. 4a, magnetite activities are calculated for spinels trending along the global trajectory in Cr#–Mg# space at constant $Fe^{3+}/\sum Fe$ ratio. At Cr# <60, both models suggest that a_{Fe3O4} decreases as Cr# increases. However, at Cr# >60, the Nell–Wood model diverges from the Sack–Ghiorso model, with the Nell–Wood model reversing slope at high Cr# such that
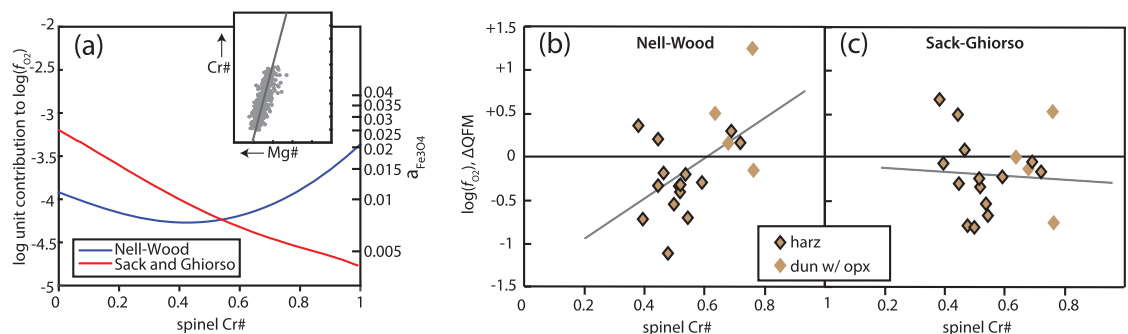
Fig. 4. Effect of magnetite activity model on calculated f_{O2}. (a) To demonstrate the effect of the activity model on calculated f_{O2}, a trajectory for model spinel compositions was calculated in Cr#–Mg# space based on the ridge peridotite array (inset) at constant $Fe^{3+}/\Sigma Fe = 0.12$. The activity of magnetite was calculated for this spinel trajectory using both the Nell–Wood model (blue line) and the Sack and Ghiorso model (red line), shown on the right axis. As activity components for each phase have an additive effect on $\log(f_{O2})$, the contribution of magnetite activity to $\log(f_{O2})$ can be calculated according to the formula $\log(f_{O2})_{contribution\_aFe3O4} = 2\log_{10}(a_{Fe3O4})$, shown on the left axis. (b, c) Literature data for the Conical Seamount (Parkinson & Pearce, 1998) as calculated in the original paper (b) compared with the data recalculated in this study (c). Trend lines show the positive correlation as described by Parkinson & Pearce for the original data and the lack of a positive correlation when the data are recalculated according to the method of Davis *et al.* (2017). Trend line for original data: $\log(f_{O2}) = 2.3Cr\# - 1.4$, $R^2 = 0.27$. Trend line for recalculated data: $\log(f_{O2}) = -0.0029Cr\# + 0.019$, $R^2 = 0.0065$.

a_{Fe3O4} increases as Cr# increases. The Nell–Wood model determines cation site occupancies based on electrical conductivity measurements in solid-solution spinels. However, Nell & Wood (1991) found that at high Cr content ($X_{FeCr2O4} > 0.6$ on the $FeCr_2O_4$–Fe_3O_4 join), the mechanism of conduction shifts from octahedral polaron hopping between Fe^{2+} and Fe^{3+} to a more complicated mechanism involving both Fe and Cr. As a result, site occupancy data for Fe^{3+} at these high Cr concentrations were excluded from their model, resulting in extrapolation of the final model to these compositions. The Sack–Ghiorso model, rather than use electrical conductivity measurements, determines site occupancy for Fe^{3+} along the $FeCr_2O_4$–Fe_3O_4 join by choosing regular solution parameters for $FeCr_2O_4$–$Fe^{2+}(Fe^{3+})_2O_4$ and $FeCr_2O_4$–$Fe^{3+}(Fe^{2+},Fe^{3+})O_4$ solid solutions such that both room-temperature site distributions and activity–composition constraints are satisfied. As the Sack–Ghiorso model avoids the extrapolation inherent in the Nell–Wood model, we determined that the Sack–Ghiorso model is more applicable than the Nell–Wood model to spinels at high Cr#, such as many forearc spinels (e.g. this study; Parkinson & Pearce, 1998; Dare *et al.*, 2009).

Parkinson & Pearce (1998) concluded that samples from the Conical Seamount, Marianas, have interacted with oxidized subduction-related melts, based partially upon a stated positive correlation ($R^2 = 0.3$) between f_{O2} and Cr# in these samples (Fig. 4b). However, when recalculated using the Sack–Ghiorso model (Fig. 4c), Conical Seamount samples at high Cr# (>60) return f_{O2} values up to a log unit more reduced than the Nell–Wood values reported in the original paper. Instead, these samples are consistent with the oxygen fugacity of Conical Seamount samples at lower Cr#, such that f_{O2} and Cr# are not correlated ($R^2 = 0.0065$).

When recalculating literature data, we included only studies that reported spinel $Fe^{3+}/\Sigma Fe$ ratios as determined

either by Mössbauer spectroscopy (Wood & Virgo, 1989; Bryndzia & Wood, 1990) or by electron microprobe analysis corrected to Mössbauer spinel standards (Parkinson & Pearce, 1998; Pearce *et al.*, 2000; Parkinson *et al.*, 2003). We included only studies that reported major element data for olivine, orthopyroxene, and spinel, and limited our scope to ridge peridotites, subduction-related xenoliths from oceanic arcs and forearc peridotites. The values for $Fe^{3+}/\Sigma Fe$ ratios in spinel reported in the original studies—and which are not changed by our recalculation—are shown in Fig. 5a. Recalculated f_{O2} values [comprising recalculation of temperature, magnetite activity, and f_{O2} according to the Davis *et al.* (2017) method] are shown in Fig. 5b and compiled in SD Electronic Appendix 4.

RESULTS

Major elements

The major element compositions of olivine, orthopyroxene, and clinopyroxene in the Tonga peridotites are similar to those of mid-ocean ridge peridotites (e.g. Dick, 1989; Warren, 2016) and key aspects of their geochemistry are summarized in Table 2.

Olivine forsterite contents average 90.9 ± 0.6 in all samples analyzed (SD Electronic Appendix 5). Olivine from one sample (BMRG08-106-1-12) consistently returned low totals and data from this sample are excluded from further discussion. Mg# [Mg# = 100Mg/ (Mg + Fe)] in orthopyroxene averages 91.3 ± 0.4 in all samples in which orthopyroxene was present (SD Electronic Appendix 6). Mg# in olivine is correlated with Mg# in orthopyroxene, suggesting that these minerals are near equilibrium. Clinopyroxene major element data were obtained for a selection of samples and are reported in SD Electronic Appendix 7.

Spinel compositions (SD Electronic Appendix 8) are variable both between and within dredges, as shown in
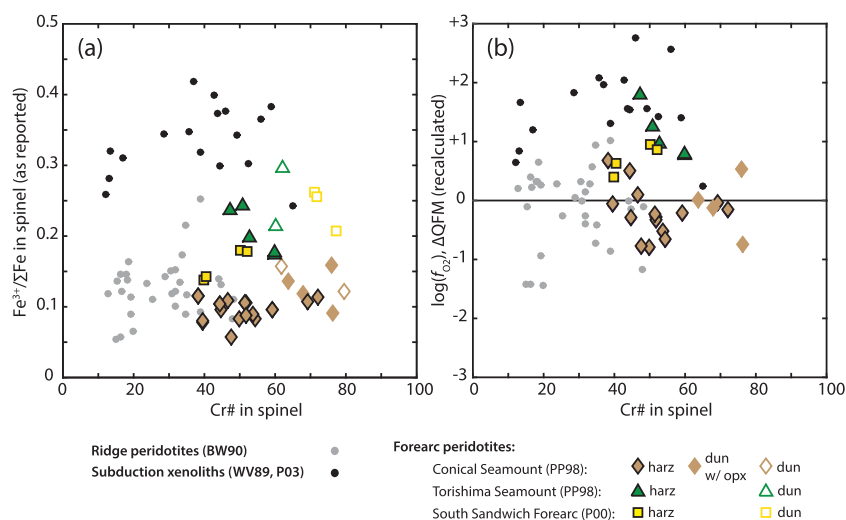
Fig. 5. Spinel $Fe^{3+}/\Sigma Fe$ ratios and peridotite f_{O_2} values for literature samples. (a) $Fe^{3+}/\Sigma Fe$ ratios in peridotite spinels from the literature. (b) Values of $\log(f_{O_2})$ for literature peridotites, recalculated according to the method of Davis *et al.* (2017). Plots of both $Fe^{3+}/\Sigma Fe$ ratio in spinel and f_{O_2} are useful, as f_{O_2} cannot be calculated when one or more phase is missing, such as occurs in dunites. Data for ridge peridotites are from Bryndzia & Wood (1990); for subduction xenoliths from Wood & Virgo (1989) and Parkinson *et al.* (2003); for forearc peridotites from Parkinson & Pearce (1998) and Pearce *et al.* (2000).

Fig. 6. Dredge BMRG08-98 has the largest range of spinel compositions, with spinel Cr# [Cr# = 100Cr/(Cr + Al)] ranging from 44 to 73 in harzburgites and from 75 to 76 in dunites. Spinels from dredge BMRG08-111 have Cr#s ranging from 46 to 61 in harzburgites, whereas the lherzolite has a Cr# of 21. Harzburgite spinels in dredges NOVA88 and 7TOW range from Cr# of 52 to 61. Spinels in dredge BMRG08-106 range from Cr# of 28 to 31 in harzburgite and 36 to 57 in dunite.

Overall, the spinel Cr# range in dredge BRMRG08-98 is large, encompassing the range in dredges 111, NOVA88 and 7TOW (Fig. 6). Dredge BMRG08-106 harzburgites are also notable in that their spinel Cr#s are significantly lower than and offset from the continuous range of Cr#s displayed in the other dredges (Fig. 6). This offset, combined with other geochemical characteristics described in more detail below, was used to establish two categories of forearc peridotite: 'Group I' (BMRG08-98, BMRG08-111, 7TOW-57, NOVA88) and 'Group II' (BMRG08-106).

Temperatures calculated using spinel–olivine thermometry average 874 ± 35°C (Table 2) and are broadly consistent with the ridge peridotite average of 940 ± 100°C [*n* = 299; data from Warren (2016)]. Temperatures calculated using pyroxene-based thermometers return higher temperatures, as discussed in Supplementary Data Section 1.

Trace elements

Trace element concentrations for clinopyroxene and orthopyroxene, as well as a limited number of olivines, are reported in SD Electronic Appendix 9. Figure 7a shows clinopyroxene trace elements normalized to Primitive Upper Mantle values of Palme & O'Neill (2014), with the element order based upon Pearce & Parkinson (1993), which places elements in order of

relative incompatibility within a spinel lherzolite. Rare earth element (REE) patterns are shown in Fig. 7b, normalized to the chondrite values of Anders & Grevesse (1989).

The rare earth element abundances of the Tonga peridotites plot in two groups that correspond to the Group I and Group II categories defined based on spinel Cr# (Fig. 6c). The Group I dredges have lower REE concentrations compared with the Group II peridotites, and abundances do not overlap between the groups (Fig. 7b). Within the trace element suite (Fig. 7a), Group I clinopyroxenes generally have lower trace element abundances than Group II clinopyroxenes, with the exception of a small positive Nb anomaly. Group II clinopyroxenes generally have a negative anomaly in Nb and Ta. In general, the distinctions between Group I samples and Group II samples is best defined by their REE patterns.

Trace element concentrations in orthopyroxene are generally lower than in clinopyroxene, with concentrations below detection for many of the light REE (LREE) and middle REE (MREE) (SD Electronic Appendix 9). Trace element concentrations in harzburgitic olivine are lower still, with most elements below detection. Trace element concentrations in dunitic olivine are moderately enriched, particularly in Rb, Ba, and U. As discussed in the Methods section, we have chosen not to interpret Pb data for our samples, because of large uncertainty stemming from potential contamination issues.

$Fe^{3+}/\Sigma Fe$ ratios in spinel and oxygen fugacity

Ferric to total iron ratios ($Fe^{3+}/\Sigma Fe$) in spinel are similar within dredges, but vary between dredges (Fig. 8a). Spinels in lherzolites, harzburgites, and dunites from Group I dredges average $Fe^{3+}/\Sigma Fe$ = 0.11 ± 0.02.

**Table 2:** Summary of results for Tonga forearc peridotites from each focus dredge

| Sample	Rock type	spinel $Fe^{3+}/\Sigma Fe$	1σ	error	a_{Fe3O4}	Cr#	1σ	Mg#	1σ	TiO_2	1σ	olivine Fo#	1σ	orthopyroxene $X^{M1} \times X^{M2}$	1σ	T (°C)	1σ	P (GPa)	log(f_{O2}) (ΔQFM)	1σ	error (+)	error (−)
111-3-6	lherz	0.16	0.02	0.02	0.014	21.2	0.7	73.7	0.7	0.085	0.006	90.36	0.08	0.00806	0.00058	917	25	0.6	0.78	0.22	0.50	0.52
111-3-1	harz	0.13	0.01	0.01	0.009	60.7	0.5	50.8	4.2	0.021	0.170	91.41	0.07	0.00686	0.00017	817	54	0.6	0.56	0.15	0.41	0.42
111-3-5*	harz	0.12	0.01	0.01	0.005	46.3	0.7	62.4	1.8	0.057	0.010	91.01	0.02	0.00696	0.00014	884	31	0.6	0.00	0.20	0.49	0.52
111-3-7	harz	0.13	0.01	0.01	0.006	61.7	1.0	53.1	0.7	0.003	0.006	91.04	0.15	0.00697	0.00002	870	15	0.6	0.11	0.09	0.42	0.44
111-3-8	harz	0.12	0.01	0.01	0.006	53.8	0.7	57.3	0.9	0.007	0.013	91.03	0.14	0.00706	0.00020	866	11	0.6	0.10	0.17	0.45	0.48
111-3-10	harz	0.14	0.01	0.01	0.009	54.6	0.8	55.6	1.4	0.007	0.012	90.69	0.05	0.00703	0.00017	865	20	0.6	0.28	0.10	0.41	0.42
106-1-2	harz	0.22	0.01	0.01	0.043	28.6	2.1	66.5	1.6	0.035	0.019	90.56	0.07	0.00857	0.00003	821	16	0.6	1.81	0.09	0.40	0.40
106-1-2*	harz	0.22	0.03	0.03	0.039	29.7	1.4	66.2	1.4	0.041	0.014	90.56	0.14	0.00799	0.00041	827	36	0.6	1.65	0.15	0.40	0.40
106-1-5	harz	0.23	0.01	0.01	0.040	28.7	1.5	66.9	0.7	0.042	0.016	90.33	0.12	0.00835	0.00009	844	21	0.6	1.63	0.11	0.39	0.40
106-1-17	harz	0.24	0.03	0.03	0.036	31.2	3.7	66.7	2.4	0.052	0.014	90.37	0.10	0.00832	0.00024	866	44	0.6	1.59	0.11	0.38	0.39
106-1-1*	dun	0.28	0.01	0.01	0.051	57.2	2.7	48.3	2.4	0.403	0.014	89.90	0.15	—	—	828	29	0.6	—	—	—	—
106-1-3	dun	0.32	0.01	0.01	0.099	36.0	1.1	58.5	1.2	0.265	0.019	89.64	0.10	—	—	815	13	0.6	—	—	—	—
106-1-15	dun	0.32	0.02	0.01	0.080	55.9	1.7	47.0	2.3	0.658	0.155	89.98	0.26	—	—	803	34	0.6	—	—	—	—
98-1-10	harz	0.10	0.01	0.01	0.004	69.1	1.3	47.1	2.0	0.035	0.005	90.96	0.10	0.00664	0.00019	849	32	0.6	−0.38	0.14	0.44	0.46
98-1-11	harz	0.12	0.01	0.02	0.004	46.6	1.4	64.4	1.1	0.024	0.005	90.66	0.13	0.00700	0.00018	943	34	0.6	−0.23	0.16	0.48	0.51
98-1-12	harz	0.09	0.01	0.01	0.003	73.3	0.6	45.8	0.6	0.033	0.007	90.93	0.11	0.00654	0.00057	863	4	0.6	−0.67	0.14	0.45	0.48
98-1-12*†	harz	0.09	0.01	0.01	0.002	73.3	0.4	46.4	0.9	0.036	0.014	*90.93*	*0.11*	0.00624	0.00016	869	12	0.6	−0.86	0.12	0.47	0.49
98-1-23	harz	0.10	0.01	0.01	0.003	66.3	1.0	52.2	0.9	0.030	0.010	90.97	0.01	0.00700	0.00038	893	7	0.6	−0.54	0.20	0.47	0.50
98-2-1*	harz	0.10	0.01	0.01	0.003	59.2	0.7	56.5	0.7	0.026	0.009	90.78	0.07	0.00680	0.00026	908	19	0.6	−0.66	0.20	0.49	0.53
98-2-3	harz	0.11	0.02	0.02	0.004	60.8	1.1	55.7	1.6	0.029	0.010	91.05	0.17	0.00648	0.00016	897	28	0.6	−0.31	0.27	0.46	0.48
98-2-6	harz	0.14	0.01	0.01	0.007	54.4	0.5	58.8	0.8	0.002	0.004	91.12	0.05	0.00648	0.00010	892	10	0.6	−0.23	0.14	0.43	0.44
98-2-7	harz	0.09	0.02	0.01	0.003	52.4	1.4	60.2	1.4	0.022	0.009	90.87	0.14	0.00652	0.00007	905	14	0.6	−0.71	0.50	0.54	0.58
98-2-8	harz	0.08	0.01	0.02	0.002	44.1	1.0	63.7	1.5	0.032	0.008	90.61	0.21	0.00714	0.00020	905	34	0.6	−0.83	0.34	0.61	0.68
98-2-10	harz	0.14	0.02	0.01	0.008	45.5	0.3	62.0	0.4	0.031	0.007	91.16	0.20	0.00641	0.00017	864	8	0.6	0.34	0.20	0.46	0.48
98-2-18	harz	0.10	0.01	0.01	0.004	46.4	0.3	61.5	1.1	0.025	0.006	90.68	0.10	0.00709	0.00021	884	19	0.6	−0.43	0.19	0.53	0.57
98-2-23	harz	0.10	0.01	0.01	0.003	49.4	0.4	62.5	1.4	0.029	0.007	90.79	0.08	0.00706	0.00054	924	24	0.6	−0.51	0.23	0.53	0.57
98-2-24	harz	0.10	0.01	0.01	0.003	70.2	1.8	47.9	0.9	0.026	0.004	90.86	0.11	0.00664	0.00019	870	11	0.6	−0.48	0.22	0.44	0.46
98-2-25	harz	0.10	0.01	0.01	0.003	56.5	0.4	58.0	1.2	0.030	0.009	90.93	0.11	0.00662	0.00015	903	16	0.6	−0.49	0.15	0.49	0.52
98-2-29	harz	0.16	0.02	0.01	0.008	47.2	0.7	63.1	1.5	0.037	0.009	90.54	0.15	0.00712	0.00012	934	34	0.6	0.27	0.20	0.42	0.43
98-1-6	dun	0.12	0.01	0.02	0.005	75.9	0.6	42.9	2.2	0.039	0.006	90.96	0.09	—	—	845	27	0.6	—	—	—	—
98-1-8	dun	0.15	0.01	0.02	0.006	74.6	1.3	50.8	3.4	0.007	0.012	92.62	0.13	—	—	865	48	0.6	—	—	—	—
98-1-9	dun	0.11	0.01	0.02	0.002	75.9	0.2	54.1	0.8	0.061	0.008	91.95	0.16	—	—	943	11	0.6	—	—	—	—
7TOW-57-1B‡	harz	0.13	0.02	0.01	0.006	55.8	1.8	56.0	1.0	0.012	0.009	91.12	0.02	0.00666	0.00027	861	21	0.6	0.17	0.37	0.44	0.45
7TOW-57-4‡	harz	0.13	0.02	0.01	0.006	57.6	0.7	55.6	1.3	0.010	0.010	91.52	0.05	0.00663	0.00016	852	17	0.6	0.38	0.38	0.49	0.45
N88-A1‡	harz	0.11	0.02	0.01	0.004	52.4	1.5	59.7	1.0	0.007	0.007	91.22	0.10	0.00642	0.00031	883	15	0.6	−0.18	0.28	0.49	0.52
N88-C1‡	harz	0.11	0.01	0.01	0.004	55.3	0.8	55.3	0.9	0.008	0.004	91.42	0.05	0.00643	0.00030	876	17	0.6	−0.11	0.12	0.46	0.49
N88-D1‡	harz	0.11	0.01	0.01	0.004	56.6	0.7	59.6	1.0	0.014	0.008	91.78	0.29	0.00673	0.00021	888	20	0.6	0.07	0.10	0.50	0.52
N88-F1‡	harz	0.10	0.01	0.01	0.003	55.5	0.9	60.1	0.6	0.009	0.007	91.75	0.08	0.00609	0.00015	888	9	0.6	−0.10	0.14	0.50	0.54

*Samples from the collection of T. Falloon.

†Thin section not analyzed for olivine; olivine analyses from another thin section from the same sample were used instead.

‡Samples obtained from H. Dick. All other samples obtained from S. Bloomer.

Cr# = 100Cr/(Cr + Al). Mg# = 100Mg/(Mg + Fe^{2+}). Fo# = 100Mg$_{ol}$/(Mg$_{ol}$ + Fe$_{ol}$). Temperatures were calculated using the olivine–spinel thermometer of Li *et al.* (1995), and log(f_{O2}) values were calculated using the oxybarometer of Davis *et al.* (2017), which is modified from the method of Mattioli & Wood (1988) and Wood & Virgo (1989).
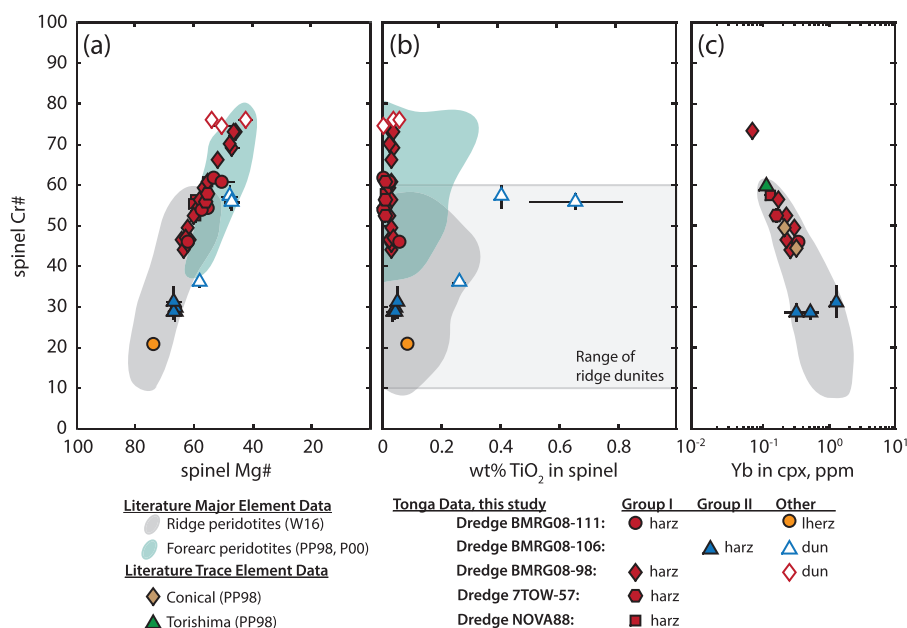
Fig. 6. Spinel systematics for Tonga peridotites compared with literature data. (a) Spinel Cr# vs spinel Mg#. (b) Spinel Cr# vs wt % TiO_2 in spinel. Dunites in ridge peridotites have spinel TiO_2 concentrations extending to 4 wt %. (c) Spinel Cr# vs Yb in clinopyroxene. Error bars represent one standard deviation for all points within a sample. Forearc data are from Parkinson & Pearce (1998) and Pearce *et al.* (2000). A limited number of single data points from the Conical and Torishima seamounts (Parkinson & Pearce, 1998) have trace element data reported; these are highlighted in (c). Ridge peridotite data are from Warren (2016).
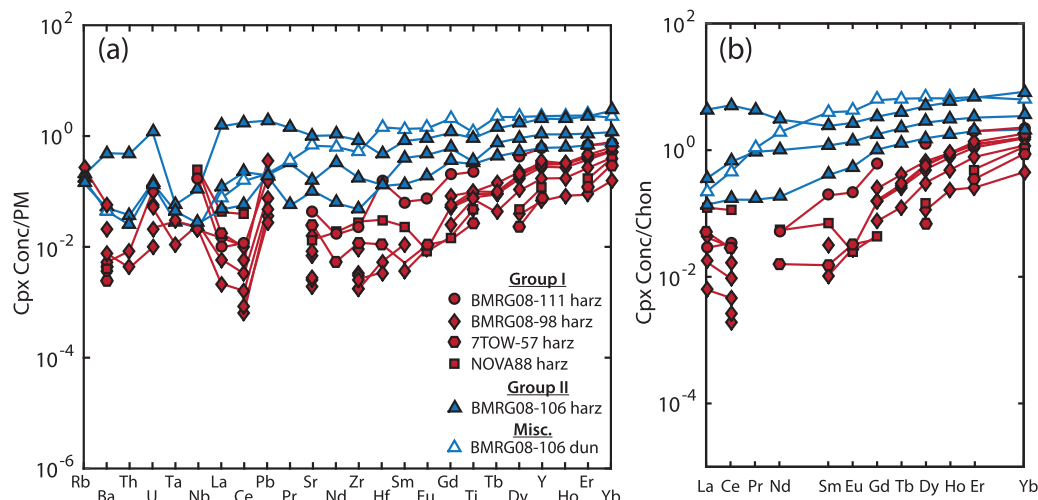
Fig. 7. (a) Clinopyroxene trace element data, normalized to Primitive Upper Mantle (Palme & O'Neill, 2014). (b) Clinopyroxene REE data, normalized to chondrite (Anders & Grevesse, 1989).

However, spinels in harzburgites from Group II samples record higher values, averaging 0.22 ± 0.01. Spinels in dunites from dredge BMRG08-106 record even higher values, averaging 0.30 ± 0.02.

Values for oxygen fugacity, calculated relative to the QFM buffer, are reported in Table 2 and shown in Fig. 8b. Harzburgites from Group I dredges average 0·2 log units (± 0.4) below QFM, whereas Group II harzburgites average 1·7 log units (± 0.1) above QFM. One lherzolite from dredge BMRG08-111 records an f_{O2} of 0·8 log units above QFM.

As the dunites in the Tonga dredges contain no orthopyroxene, the equilibrium assemblage that fixes oxygen fugacity is not present and spinel oxybarometry

cannot be used to calculate f_{O2} for these samples. For this reason, Fig. 8 shows both the $Fe^{3+}/\Sigma Fe$ ratio in spinel and f_{O2} for the subset of samples containing olivine, orthopyroxene, and spinel, because the relationship between $Fe^{3+}/\Sigma Fe$ and f_{O2} is not constrained when one or more phase is missing.

In comparison with literature data, Group I harzburgites have spinel Mg#–Cr# values that extend to higher Cr# than the ridge peridotite array, but overlap the forearc peridotite array, whereas Group II harzburgite spinels plot within the ridge peridotite array (Fig. 6). The $Fe^{3+}/\Sigma Fe$ ratios and f_{O2} values of Group I spinels extend from the mid-ocean ridge peridotite array up to higher
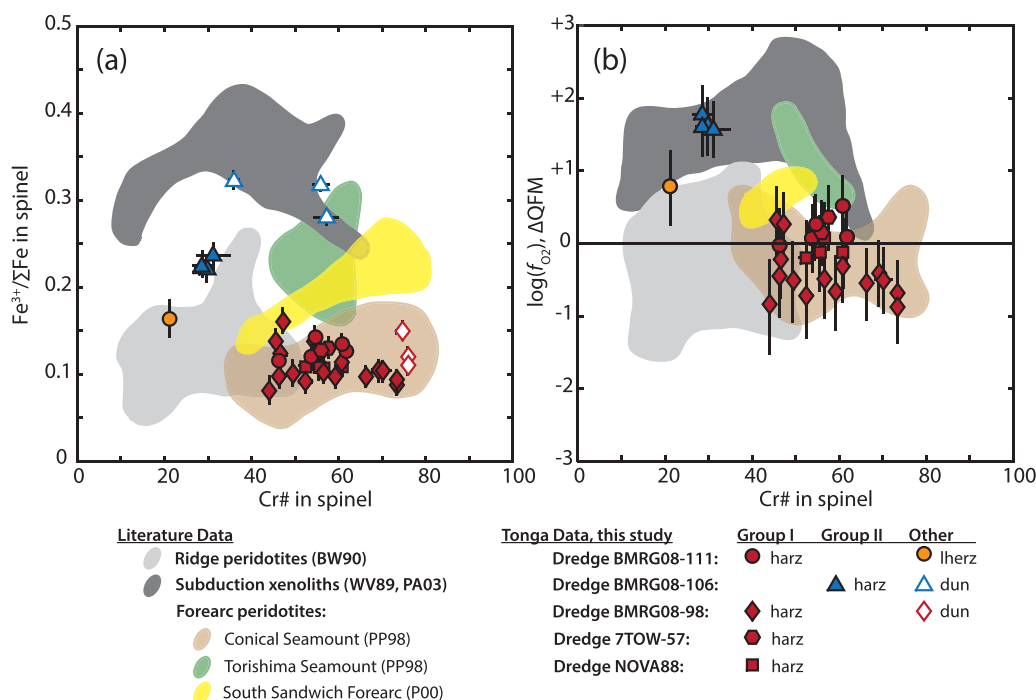
Fig. 8. (a) $Fe^{3+}/\Sigma Fe$ ratios in spinel vs Cr# in spinel for samples from this study. (b) $\log(f_{O2})$ results for samples from this study. Background fields represent literature data, as shown in Fig. 5, for peridotites and dunites in (a) and for peridotites only in (b). Dredges from this study are classified as Group I if the harzburgites have high Cr# and low $\log(f_{O2})$ and as Group II if they have lower Cr# and higher $\log(f_{O2})$. Error bars represent total uncertainty for $Fe^{3+}/\Sigma Fe$ and $\log(f_{O2})$, and one standard deviation for all points within a sample for spinel Cr#.

Cr# values (Fig. 8). In marked contrast, the Group II harzburgites have lower spinel Cr# and elevated spinel $Fe^{3+}/\Sigma Fe$ ratios and f_{O2}. These samples are more oxidized than the mid-ocean ridge peridotite array, with f_{O2} more similar to the subduction-zone xenolith array (Fig. 8).

Categorization of Tonga peridotites

As described above, we have categorized the Tonga peridotites into two groups based on spinel Cr#, f_{O2}, and trace element concentrations.

1. Group I peridotites comprise harzburgites from dredges BMRG08-98, BMRG08-111, NOVA88, and 7TOW-57. These samples extend to high spinel Cr# (Cr# = 44–73) at relatively low f_{O2} (−0·2 log units, ±0·4, relative to QFM) (Fig. 8) and have extremely depleted trace element concentrations (Fig. 7), with the exception of a small positive Nb anomaly.
2. Group II peridotites comprise harzburgites from dredge BMRG08-106. These samples have lower spinel Cr# (Cr# = 28–31) at elevated f_{O2} (+1·7 log units, ±0·1, relative to QFM) (Fig. 8) and have higher trace element abundances in general than the Group I samples (Fig. 7).

DISCUSSION

Our results indicate that the Tonga forearc is heterogeneous with respect to oxygen fugacity on a spatial scale of hundreds of kilometers, varying by over two log units

between dredges (Fig. 8). This heterogeneity between dredges must be due to a different geochemical history for the two groups of samples, related either to the original mantle source or to one or more processes occurring prior to their emplacement in the trench. Below, we derive interpretations for the two primary groups of Tonga peridotites—defined above based on their geochemical systematics—in the context of the likely mantle processes that occurred prior to emplacement of these rocks in the modern Tonga forearc.

Group I: residues of high extents of fractional decompression melting

We interpret Group I peridotites (harzburgites from BMRG08-98, BMRG08-111, 7TOW-57, NOVA88) to be the residues of large degrees of near-fractional melting, with little subduction influence, which most probably formed during the first stages of subduction initiation.

Spinels in Group I are broadly consistent with the global trend between spinel Cr# and Mg#, but they extend to higher values than the mid-ocean ridge peridotite array (Fig. 6a). Spinel Cr# is traditionally used as a proxy for degree of melt extraction, owing to the preferential removal of Al over Cr from spinel during melting (Dick & Bullen, 1984). In ridge peridotites, spinel Cr#s range from ~10 up to ~60. Modeling of near-fractional melting suggests that a spinel Cr# of 60 is an upper boundary that corresponds to about 18–20% melt extraction, near the clinopyroxene-out transition (e.g. Hirschmann *et al.*, 1998; Warren, 2016). The lack of

ridge peridotites with spinel Cr#s higher than this value has been attributed to the sharp decrease in melt productivity once clinopyroxene is exhausted (e.g. Hirschmann *et al.*, 1998). Spinel Cr#s higher than 60 may be due either to extremely large degrees of melting, almost certainly past clinopyroxene-out, or to melt–rock interaction with Cr-rich melts (e.g. Parkinson & Pearce, 1998; Pearce *et al.*, 2000; Morishita *et al.*, 2011).

We attribute the high spinel Cr#s in the Group I samples to large degrees of melting, rather than interaction with Cr-rich melts. We find that progressive depletion in the heavy REE (HREE) is well correlated with an increase in spinel Cr# (Fig. 6c), consistent with large degrees of melt extraction (e.g. Batanova *et al.*, 1998; Hellebrand *et al.*, 2001; Warren, 2016). Petrographically, the interpretation that high spinel Cr#s suggest that melting has continued past clinopyroxene-out in these samples is supported by the absence of clinopyroxene in thin sections for samples with Cr# >60 and the lack of melt enrichment textures such as veins, plagioclase, sieve-textured spinels, or inclusions within orthopyroxene (e.g. Seyler *et al.*, 2004, 2007; Shaw & Dingwell, 2008; Tollan *et al.*, 2015; Warren, 2016).

If the high Cr#s in Group I peridotites are due to interaction with melt, we would expect to see strong enrichments in LREE and fluid-mobile elements (FME). To model the clinopyroxene trace element patterns observed in the Group I harzburgites, we first applied a standard non-modal fractional melting model (Shaw, 1970; Johnson *et al.*, 1990) to the Group I REE patterns using parameters from Warren (2016) (see Supplementary Data, Section 2). Whereas HREE and MREE in all samples are well matched by large degrees of fractional melting (up to a melt fraction of 18%, approaching cpx-out), enrichments in LREE cannot be explained by this model (Fig. 9). LREE enrichments are

seen frequently in ridge peridotites (Warren, 2016) and are attributed to either interaction with small amounts of melt (e.g. Brunelli *et al.*, 2006; Seyler *et al.*, 2007; Godard *et al.*, 2008; Warren, 2016) or disequilibrium melting, in which the kinetics of REE exchange between mineral and melt are slow compared with the melting rate (e.g. Van Orman *et al.*, 2002; Liang & Liu, 2016). Thus, to assess the LREE enrichments in our samples, we applied both a disequilibrium melting model and a simple melt addition model to the Group I samples.

To model disequilibrium melting for our samples, we used the model of Liang & Liu (2016), which introduces a parameter, ε, to quantify the degree of disequilibrium for an element of interest. Liang & Liu (2016) used the parameter ε_{La}, representing the ratio of bulk melting rate to mineral–melt exchange rate for La, to assess disequilibrium melting in natural samples. Code for implementing this model was kindly provided by Yan Liang. For consistency, we amended the code to use the same initial mineral modes, partition coefficients, and melt reaction modes as the fractional melting model described above (see Supplementary Data Section 2).

To model melt addition, we developed a simple, closed-system melt re-impregnation model that we applied to both the REE and a suite of fluid-mobile elements (Ba, Pb, and Sr) and high field strength elements (HFSE; Nb, Zr, Ti, Y). As melts or fluids with enriched incompatible trace element concentrations interact with a depleted residual peridotite during flux melting, reactive porous flow, or melt re-impregnation, the peridotite will become enriched in these incompatible elements. The magnitude of this enrichment depends on the amount of melt added as well as the concentration of each trace element in the melt. In the case of flux melting [in which the peridotite's solidus is lowered owing to the

Group I Peridotites
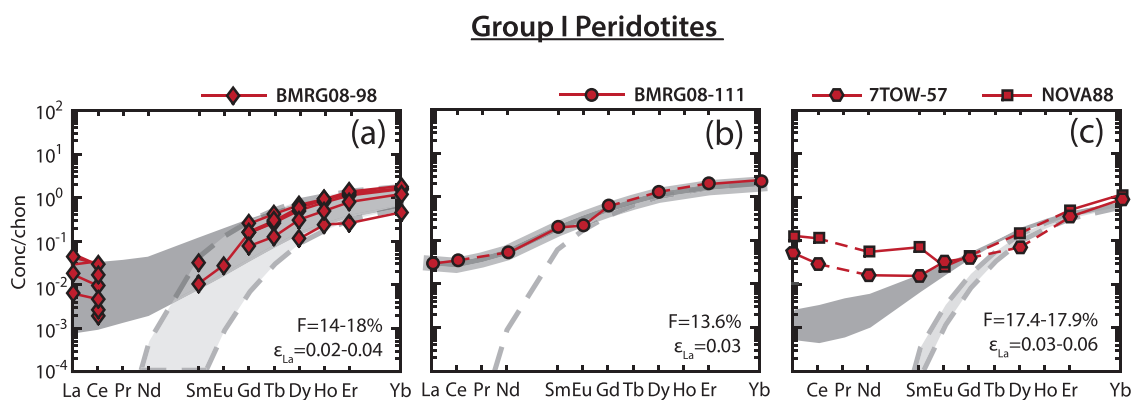
Fig. 9. Model results for disequilibrium melting for clinopyroxene for REE in Group I peridotites. The disequilibrium melting model is from Liang & Liu (2016; see Supplementary Data Section 2 for model parameters). Dashed lines and light grey fields are fractional melting only; continuous lines and dark grey fields are fractional melting plus disequilibrium melting. Concentrations are shown normalized to chondrite (Anders & Grevesse, 1989). (a) Model results for clinopyroxenes from six harzburgites from dredge BMRG08-98. MREE and HREE patterns are well matched by large degrees of fractional melting (to near cpx-out). LREE require enrichment relative to fractional melting and are well matched by disequilibrium melting. (b) Model results for clinopyroxene from dredge BMRG08-111 harzburgites. Dredge BMRG08-111 is well matched by ∼14% fractional melting at ε_{La} = 0·03. (c) Model results for clinopyroxene from dredges 7TOW-57 and NOVA88. Whereas HREE in these dredges are well matched by disequilibrium melting, LREE are very poorly matched, suggesting that LREE enrichment in 7TOW-57 and NOVA88 samples is not the result of disequilibrium melting.

presence of aqueous fluid (e.g. Tatsumi *et al.*, 1983)] or reactive porous flow [in which a pyroxene-undersaturated melt dissolves pyroxene from a peridotite to form dunite (e.g. Kelemen *et al.*, 1995)], the melt or fluid that enters the system also leaves the system after having interacted and equilibrated with the solid. As a result, modeling these processes can be very complex as thermodynamic properties such as phase saturation and melt reaction modes for the melt and solid are needed. To maximize the simplicity of our model and limit the number of unconstrained parameters, we decided to model melt addition as a simple, closed-system melt re-impregnation process based on mass-balance of trace elements in the residue, the infiltrating melt, and the partition coefficients between phases. As described in Supplementary Data Section 2, our model inputs clinopyroxene trace element concentrations and the trace element concentrations of a spatially associated lava. The model optimizes (1) the degree of fractional melting of an initial depleted MORB mantle (DMM) source and (2) the amount of melt added to find the best fit between the input clinopyroxene trace element pattern and the modeled result.

LREE enrichments in the majority of Group I Tonga peridotites are well described using either the disequilibrium melting model (Fig. 9) or the melt addition model (Fig. 10). If these samples have indeed been re-enriched with melt, it is in extremely small quantities (<0·005%), and probably has at most a minor effect on major element chemistry or recorded f_{O2}. Among the FME and HFSE, we did not assess disequilibrium melting owing to a lack of constraints on diffusion rates for these elements. The FME and HFSE concentrations predicted by our melt addition model are in partial agreement with our Group I data. Our samples tend to have lower Ti and Y than predicted by the model and sharp positive Nb anomalies. At the very high Cr content of our Group I pyroxenes, very low Nb concentrations could be affected by a polyatomic interference of $^{40}Ar^{53}Cr$ on ^{93}Nb. We found this interference to be negligible in reference glasses up to 2500 ppm Cr, but cannot rule it out at higher Cr concentrations. Alternatively, the Nb spikes could be due to disequilibrium melting or other mantle processes that are not yet well understood.

In all, we cannot conclusively distinguish between disequilibrium melting and small amounts of melt addition for the Group I peridotites. Additionally, the small amount of melt addition implied by our model makes it difficult to conclusively determine the identity of any interacting melt. The samples are only slightly better matched by addition of a boninite than by addition of a mid-ocean ridge basalt (Fig. 10a and b). This suggests that interaction with a subduction-related melt is not necessary to develop the trace element patterns seen in our Group I clinopyroxenes.

Although boninitic melt is not necessary to explain the observed clinopyroxene trace element patterns, we nevertheless cannot conclusively show that a boninitic

melt or fluid was not involved. For a subset of the Group I samples (primarily dredges 7TOW-57 and NOVA88), our fractional melting model cannot reproduce the observed extremely low HREE concentrations, as our model exhausts clinopyroxene before these values are reached (Fig. 10d). Hydrous melting models (e.g. Gaetani & Grove, 1998) predict that clinopyroxene will be consumed more slowly than during anhydrous melting, which could allow Group I samples to more easily reach higher degrees of melting before exhausting clinopyroxene. However, trace element compositions for the aqueous fluids involved in boninite production are poorly constrained, making it difficult to assess whether hydrous melting in the presence of such a fluid could result in the observed trace element patterns.

Thus we conclude that the Tonga Group I samples show no conclusive evidence for interaction with subduction-zone melts or fluids, and are instead most probably residues of large degrees of near-fractional melting. The extreme depletion seen in the Group I peridotites probably happens in a suprasubduction-zone setting, during the first stages of subduction initiation. Under the subduction initiation model of Reagan *et al.* (2010), the first stage of subduction results in large amounts of decompression melting in the fore-arc, as asthenospheric mantle upwells to fill in the gap left by the foundering slab. Evidence for this hypothesis comes from the presence of relatively MORB-like basalts at the base of the volcanic stratigraphy in the Mariana forearc, which has been sampled in more detail than Tonga. These forearc basalts (FAB) appear to be the product of decompression melting and lack the trace element signatures associated with subduction fluids (Reagan *et al.*, 2010). HFSE and REE patterns (Reagan *et al.*, 2010) and Y/Zr ratios (Arculus *et al.*, 2015) suggest a more refractory source for FAB than MORB, and X-ray absorption near-edge spectroscopy (μ-XANES) analyses of FAB glasses suggest that these lavas are not oxidized above ridge lavas (Brounce *et al.*, 2015).

Altogether, the extreme depletion and low f_{O2} observed in FAB make them an excellent candidate for the melts extracted from our Group I peridotites. Similar basalts have been documented within two dredges in the Tonga forearc, but they record ages prior to subduction initiation, suggesting a different petrogenesis (Falloon *et al.*, 2014). Although we favor the subduction initiation hypothesis for Group I peridotites, we cannot rule out the possibility that these samples instead represent pre-existing lithosphere (e.g. Parkinson & Pearce, 1998). However, melt depletion during subduction initiation is the simplest model in terms of emplacement of these samples into the forearc.

In summary, we propose that the petrography, oxygen fugacity and major and trace element analyses for Tonga Group I peridotites support the hypothesis that extremely refractory forearc peridotites are residues of large degrees of near-fractional, ridge-like melting, with

Group I Peridotites

Dredge BMRG08-98

Dredges BMRG08-111, 7TOW-57, NOVA88
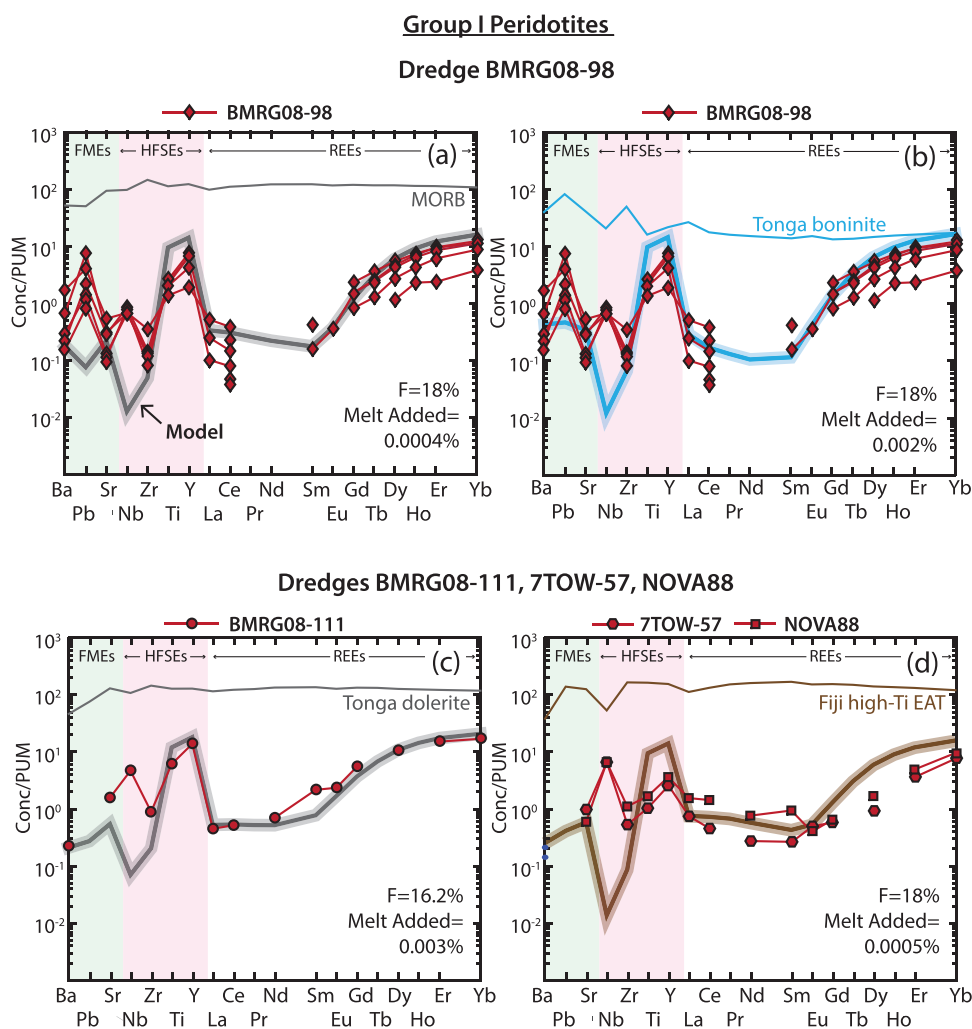
Fig. 10. Model results for melting and melt addition for extended clinopyroxene trace element patterns in Group I samples. Melt model is described in Supplementary Data Section 2. Red symbols are clinopyroxene trace element compositions for peridotites from this study. Fine continuous lines show melt trace element compositions from the literature. Bold continuous lines with shaded outline show model results for clinopyroxene compositions. Data are normalized to Primitive Upper Mantle (Palme & O'Neill, 2014). (a, b) Model results for dredge BMRG08-98 for addition of a MORB melt (Gale *et al.*, 2013) in (a) and a boninitic melt (Meffre *et al.*, 2012) in (b) to a highly refractory residue. In both (a) and (b), the patterns are relatively well matched by the model, with the exception of Pb and Nb, which show positive anomalies. The similarity in model output regardless of input melt composition demonstrates the difficulty in identifying the type of interacting melt at very small degrees of melt–rock interaction. (c) Model results for dredge BMRG08-111. The trace element pattern is best matched by large degrees of fractional melting combined with addition of a small amount of basaltic melt (Falloon *et al.*, 2014). However, as illustrated in (a) and (b), it can be difficult to distinguish between different types of melts at low degrees of melt addition. Similar to the dredge BMRG08-98 samples, a positive Nb enrichment is observed, suggesting that Group I peridotites may be recording an additional process not described by our model. (d) Model results for dredges 7TOW-57 and NOVA88, both of which are best matched by large degrees of fractional melting combined with addition of a small amount of arc tholeiitic melt (Todd *et al.*, 2012). Our model overestimates the least incompatible elements (HREE, Ti, Y) at the point of clinopyroxene-out. Nb and Zr both show a positive enrichment compared with our model.

little evidence for interaction with subduction-influenced melts or fluids.

Reassessment of Conical Seamount data from *Parkinson & Pearce (1998)*
The recalculation of literature f_{O_2}, along with our framework for trace element modeling, allows us to reassess previously published forearc peridotite data. Parkinson & Pearce (1998) reported major element, trace element, and oxygen fugacity data for two seamounts in the Izu–Bonin–Mariana arc system. Values of f_{O_2} for peridotites

from the Torishima Seamount in the Izu–Bonin forearc change only moderately upon recalculation (recalculated average of QFM + 1·17, compared with the original published value of QFM + 1·13). However, samples from the Conical Seamount in the Mariana forearc change by −0·4 to + 0·7 log units upon recalculation, with the magnitude of this change dependent on the spinel Cr# of the sample, as shown in Fig. 4c. As a result, the conclusions drawn by Parkinson & Pearce (1998) for these samples require revisiting.

Similar to our Group I peridotites, samples from the Conical Seamount record high spinel Cr#s (Cr# = 38–72)

for Conical Seamount harzburgites. Based on trace element and oxygen fugacity constraints, this signature was interpreted by Parkinson & Pearce (1998) as developing as a result of interaction of a harzburgitic residue with an oxidized boninitic melt in a suprasubduction-zone setting. Our recalculated f_{O2} results for the Conical Seamount samples, however, suggest that these peridotites are relatively reduced even at high Cr#s (Figs 4b and 5b). These f_{O2} values are consistent with the mid-ocean ridge peridotite array of Bryndzia & Wood (1990), with no oxidized signature to tie their petrogenesis to interaction with subduction-related melts.

Parkinson & Pearce (1998) used enrichments in incompatible elements such as Sr and Ce to argue for interaction with oxidized suprasubduction-zone melts, based on the concentrations of a limited number of trace elements in clinopyroxene within two of their Conical Seamount samples [initially reported by Parkinson *et al.* (1992)]. However, our trace element modeling of these two samples shows that interaction with boninitic melt is not necessary to explain the enrichments in LREE (Fig. 11). The more depleted sample is better described by disequilibrium melting (Fig. 11a) than by melt addition (Fig. 11b), whereas the less depleted sample is equally well described by either model. Additionally, within the melt addition model, the less depleted sample can be described by adding either a small amount of boninitic melt or a small amount of basaltic melt, suggesting that the interacting melt is not
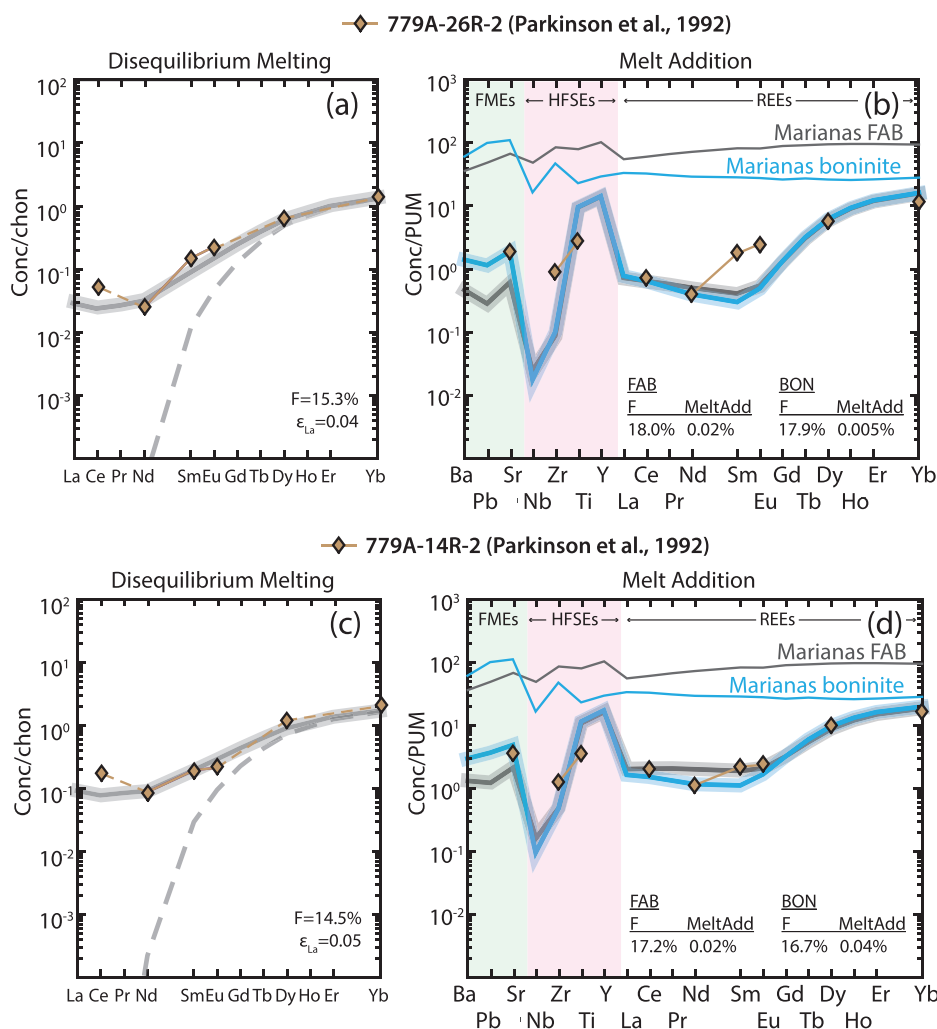
Fig. 11. Disequilibrium melting and melt addition results for clinopyroxene in harzburgites from the Conical Seamount in the Marianas (data from Parkinson *et al.,* 1992). (a) Disequilibrium melting model results for sample 779A-26R-2. The sample is well matched by ~15% fractional melting at $\varepsilon_{La} = 0.04$. (b) Melt addition model results for sample 779A-26R-2, comparing the effects of adding a boninitic melt versus a basaltic melt. Both melt compositions are from Reagan *et al.* (2010). Either of the two melts can match the HREE and LREE, whereas only the boninitic melt matches Sr, and neither melt matches Zr, Ti, and the MREE. (c) Disequilibrium melting model results for sample 779A-14R-2. The sample is well matched by 14·5% fractional melting at $\varepsilon_{La} = 0.05$. (d) Melt addition model results for sample 779A-14R-2, comparing the effects of adding the same boninitic and basaltic melts as in (b). The sample is well matched by addition of either melt for REE and Sr, but poorly matched for Zr and Ti.

necessarily an oxidized melt with a strong subduction component.

In summary, we find that the Conical Seamount trace element patterns do not show conclusive evidence for interaction with a boninitic melt in a suprasubduction-zone setting. Trace element modeling and recalculation of f_{O2} for these samples instead suggests that they most probably did not interact with oxidized melts. We interpret the high spinel Cr#s in these samples to be due to large degrees of near-fractional melting, and thus categorize the Mariana forearc samples from the Conical Seamount with our Group I peridotites.

Group II: residues of fluid-fluxed melting of a fertile mantle

We interpret Group II peridotites (harzburgites from dredge BMRG08-106) to have formed during flux melting of fertile mantle owing to interaction with subduction-related fluids and/or melts. We additionally suggest that this interaction resulted in oxidation of the peridotite residue.

The lower spinel Cr#s displayed by Group II peridotites compared with Group I peridotites (Fig. 6a) suggest that they underwent lower degrees of partial melting. However, the high LREE/HREE ratios of the Group II samples (Fig. 7) require addition of a trace element-enriched melt or fluid. Fluids and melts can interact with the mantle wedge in two distinct manners. In one scenario, fluids and hydrous melts percolate through the mantle wedge to depress the mantle solidus and cause flux melting (e.g. Tatsumi *et al.*, 1983). The melts produced mingle with the original fluxing material and then ascend to the surface as arc magmas enriched in fluid-mobile elements (Elliott *et al.*, 1997), leaving behind a residue that is also enriched in these elements. The alternative scenario is that late-stage hydrous melts can re-impregnate peridotites, such that—rather than the melt leaving the system—the melt reacts with the ambient mantle and crystallizes, thereby locally refertilizing the mantle (e.g. Dick, 1989; Seyler *et al.*, 2007; Warren, 2016).

Both scenarios are expected to result in a residue that is enriched in the same elements as the original melt or fluid, although we expect melt re-impregnation to produce additional petrographic evidence such as plagioclase, increased pyroxene content and veins. These features are absent in the Group II peridotites, and we thus consider it more likely that they are the residues of flux melting. However, as we expect both scenarios to have similar effects on trace element compositions, and the compositions of primary slab fluids are poorly constrained, we apply our simple melt-addition trace element model to the Group II peridotites. We do not employ more complex models, nor do we apply hydrous melting modes to these samples, for several reasons. We prefer to minimize the number of unconstrained parameters and maintain consistency between our modeling of Group I and Group II peridotites. We find that more complex models are not required, as our simple model reproduces the observed trace element patterns in Group II samples and allows us to conclude that these peridotites have interacted with subduction-related melts and/or fluids.

In applying our model, we tested 11 natural melts with compositions taken from the literature that are spatially or petrologically associated with the Tonga forearc. These lavas comprise boninites, arc tholeiites, basalts, dolerites, and adakites with compositions from Falloon *et al.* (2008), Meffre *et al.* (2012), Todd *et al.* (2012), Falloon *et al.* (2014), and Gale *et al.* (2013) (SD Electronic Appendix 11). Additionally, we tested a computed melt composition calculated to be in equilibrium with clinopyroxene found in a dunite from dredge BMRG08-106 (SD Electronic Appendix 11). As dunites are often interpreted as melt localization channels (Kelemen *et al.*, 1995), clinopyroxene in these samples likely crystallized from a pyroxene over-saturated melt, and thus provides constraints on melt composition. We tested each of these melts against each of the three clinopyroxene REE patterns for dredge BMRG08-106 harzburgites (BMRG08-106-1-2, BMRG08-106-1-5, and BMRG08-106-1-17).

The trace element patterns in clinopyroxene from all three Group II harzburgites can be well matched by moderate degrees of fractional melting ($\sim$14–16%) combined with addition of an arc tholeiitic melt (Fig. 12a–c). The two lava types that provide the best match are island arc tholeiites from Tonga (Meffre *et al.*, 2012) and early arc tholeiites from Fiji (Todd *et al.*, 2012). The island arc tholeiites are spatially close to dredge BMRG08-106 samples (within $\sim$100 km) and are some of the most prevalent lavas in the Tonga forearc (Meffre *et al.*, 2012). These lavas are estimated to have erupted within the first 10 Myr after subduction initiation, based on ^{40}Ar–^{39}Ar ages of 43 Ma (Meffre *et al.*, 2012). Although the early arc tholeiites are located significantly to the west of the BMRG08-106 peridotites, they are also interpreted as being associated with subduction initiation at the Tonga Trench, before the opening of the Lau Basin (Todd *et al.*, 2012).

We conclude from the trace element modeling that the Group II peridotites have interacted with arc tholeiites. These lavas are strongly subduction-associated, as they are interpreted to have formed as a result of interaction of subduction fluids with the mantle wedge. Although f_{O2} is not constrained for any of the lavas used as input compositions in our model, results from the Mariana forearc (Brounce *et al.*, 2015) suggest that lavas become more oxidized as subduction initiation proceeds and their slab component increases, with magmatic f_{O2} increasing by more than a log unit from FAB to boninites and arc lavas. This is consistent with the global observation that arc lavas are more oxidized than mid-ocean ridge lavas (e.g. Carmichael, 1991; Kelley & Cottrell, 2009; Brounce *et al.*, 2014; Grocke *et al.*, 2016) and that subduction-related xenoliths are more oxidized than ridge peridotites (Wood & Virgo, 1989;

Group II Peridotites
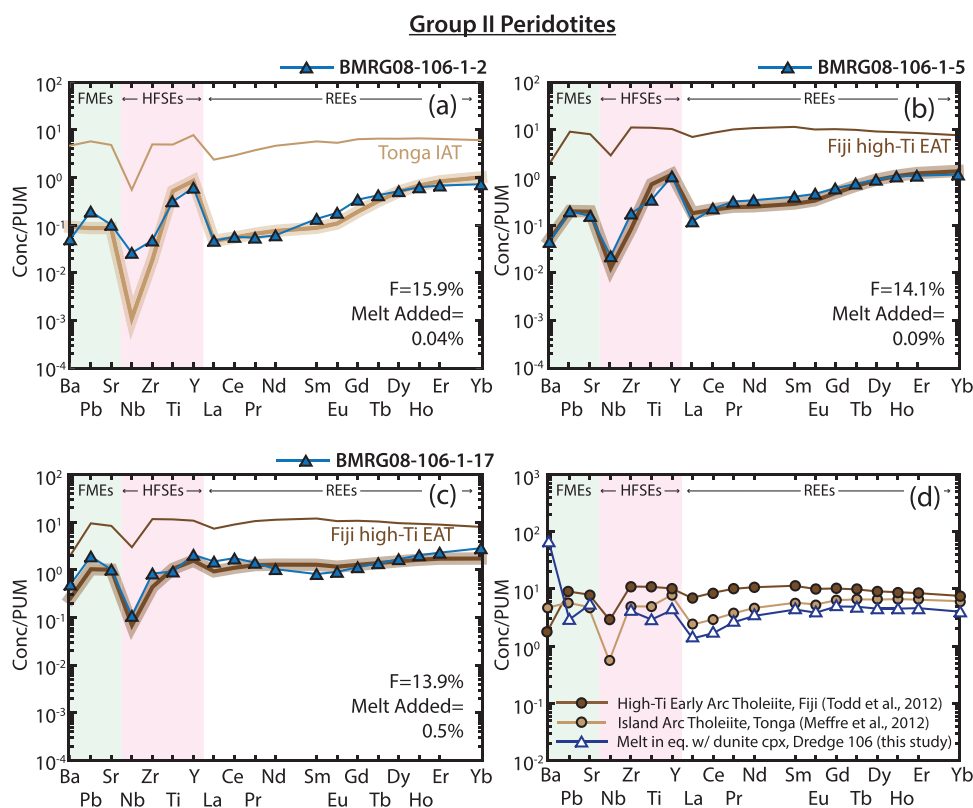
Fig. 12. Model results for melting and melt addition for extended clinopyroxene trace element patterns in Group II samples. Melt model is described in Supplementary Data Section 2. Fine continuous line without symbols is the melt composition that is added to the fractionally melted peridotite residue. The bold continuous line with shaded outline represents the model results. (a) Model results for sample BMRG08-106-1-2. The trace element pattern is well matched by moderate degrees of fractional melting combined with addition of an island arc tholeiitic melt (Meffre *et al.*, 2012). Small anomalies in Nb and Pb are seen in comparison with our model. (b) Model results for sample BMRG08-106-1-5. The trace element pattern is extremely well matched by moderate degrees of fractional melting combined with addition of an early arc tholeiitic melt (Todd *et al.*, 2012). (c) Model results for sample BMRG08-106-1-17. The trace element pattern is well matched by moderate degrees of fractional melting combined with addition of the same early arc tholeiitic melt as in (b). (d) Comparison of arc tholeiite compositions with calculated melt in equilibrium with clinopyroxene from a Group II dunite. The equilibrium melt composition was determined using clinopyroxene/melt partition coefficients, which are reported in SD Electronic Appendix 11. The calculated melt has a trace element pattern that is similar to the arc tholeiites from Tonga (Meffre *et al.*, 2012) and Fiji (Todd *et al.*, 2012) that were added to match the harzburgite patterns in (a)–(c). Whereas the calculated melt shows a distinct enrichment in Ba compared with the specific melts modeled here, other arc tholeiites reported by Meffre *et al.* (2012) and Todd *et al.* (2012) have higher Ba consistent with the concentrations measured in this sample.

Wood *et al.*, 1990; Parkinson & Arculus, 1999; Parkinson *et al.*, 2003). We therefore predict that the arc tholeiites found in the Tonga forearc are also oxidized relative to MORB.

The high f_{O_2} recorded by Group II peridotites is probably due to interaction with oxidized arc-related tholeiites in the forearc. Once corner flow is established following subduction initiation, fertile asthenospheric mantle is brought into the forearc region (Reagan *et al.*, 2015). As the subducting slab begins to dehydrate, it releases fluids into the mantle wedge, which then cause flux melting in these more fertile peridotites. Although the fluxing of fluid is expected to result in large degrees of melting within the core of the mantle wedge, the Group II peridotites must have come from near the top of the wedge to later be exposed within the trench. As the top of the wedge is cooler than the wedge core, the Group II peridotites thus experienced only moderate degrees of melting. If the fluxing fluids are oxidized (e.g. Kelley & Cottrell, 2009), fluid-induced flux melting

would probably result in the production of oxidized arc melts. Our results suggest that the process of flux melting leaves behind an oxidized peridotite residue enriched in LREE and fluid-mobile elements.

Dunites: residues of melt transport

Dunites have been found in the Tonga forearc in dredges of both Group I samples (BMRG08-98) and Group II samples (BMRG08-106), of which three from each dredge were analyzed in this study. These samples contain no orthopyroxene and extremely rare clinopyroxene, and are interpreted as residues of melt extraction channels (e.g. Kelemen *et al.*, 1995). As these samples do not include orthopyroxene, the phase assemblage required to constrain oxygen fugacity is not present. However, it is notable that their geochemistry mirrors that seen in harzburgites within the same dredge.

Dunites associated with the Tonga Group I samples and the Parkinson & Pearce (1998) Conical Seamount
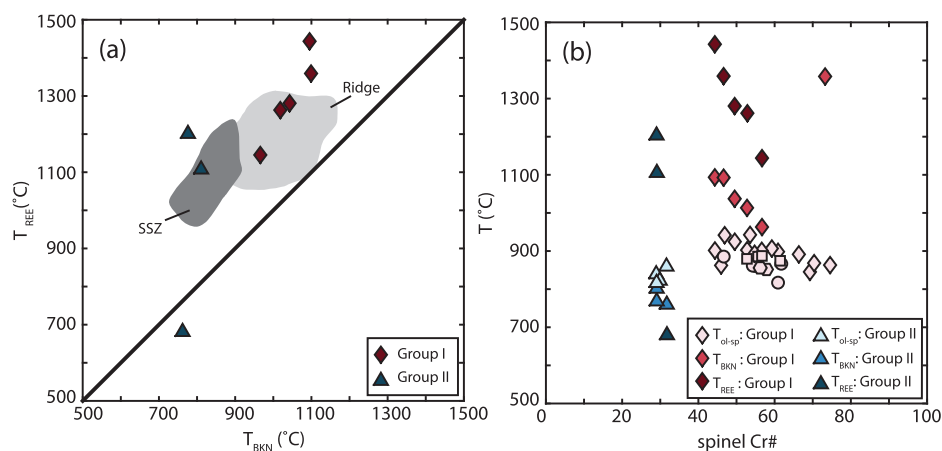
Fig. 13. Thermometry results for Tonga peridotites. (a) Temperatures based on REE exchange between clinopyroxene and orthopyroxene (T_{REE}; Liang *et al.*, 2013), compared with temperatures based on major element exchange between clinopyroxene and orthopyroxene (T_{BKN}; Brey & Köhler, 1990). The offset between T_{REE} and T_{BKN} for the majority of our samples suggests that they cooled relatively quickly. The low T_{REE} for a single Group II sample suggests that the temperature for this sample has been reset. Fields for ridge and suprasubduction-zone peridotites are from Dygert & Liang (2015). (b) Results from the three thermometers plotted with respect to spinel Cr#. Whereas temperatures based on Fe^{2+}–Mg exchange between olivine and spinel (T_{ol-sp}; Li *et al.*, 1995) for Group I peridotites are relatively consistent, T_{BKN} and T_{REE} show a sharp decrease with increasing Cr#.

samples are characterized by spinel with high Cr# (~75 for Tonga samples, 62–80 for Conical Seamount samples) and low $Fe^{3+}/\Sigma Fe$ ratios, similar to the mid-ocean ridge peridotite array (Fig. 8a). Although the high spinel Cr#s and low spinel TiO_2 concentrations (Fig. 6b) are initially suggestive of interaction with a boninitic melt, Brounce *et al.* (2015) showed that boninitic lavas in the Marianas record $Fe^{3+}/\Sigma Fe$ ratios from ~0·24 to 0·26, about 50% higher than MORB. Thus, we consider it more likely that these dunites formed as a result of interaction with late aliquots of extremely depleted forearc basalts, which may have lower TiO_2 and higher Cr# than MORB owing to depletion of incompatible elements by previous melting events.

Dunites associated with Group II samples are offset to lower spinel Mg# (Fig. 6a), with high spinel TiO_2 concentrations (Fig. 6b) and high $Fe^{3+}/\Sigma Fe$ ratios in spinel (Fig. 8a). In Fig. 12d, we show the trace element composition of the calculated melt in equilibrium with clinopyroxene found in dunite from dredge BMRG08-106. This melt is similar to both types of arc tholeiites, suggesting that these samples represent melt channels that have equilibrated with oxidized arc tholeiitic melts.

Thermal history and effects of subsolidus cooling

On average, Group II peridotites record lower temperatures than Group I peridotites for each of the three thermometers used in this study (SD Electronic Appendix 10), suggesting a different thermal history for the two groups. Although lower on average, the ranges of temperatures based on olivine–spinel thermometry and REE thermometry for Group II peridotites overlap the ranges for Group I peridotites, whereas temperatures based on pyroxene major element thermometry are significantly lower for Group II peridotites than Group I peridotites (Fig. 13). Mineral chemistries

recorded at the surface are a function of cooling rate, as chemical subsystems have different closure temperatures. For instance, the relatively high temperatures recorded by REE thermometry (SD Electronic Appendix 10; Fig. 13) result from the slow diffusion of REE compared with smaller, more mobile elements (e.g. Liang *et al.*, 2013; Dygert & Liang, 2015). The lower temperatures recorded by Group II peridotites thus may indicate that these samples cooled more slowly than Group I samples.

Although subsolidus cooling alters mineral chemistries, a difference in cooling rate cannot account for the chemical differences that we see between Group I and Group II peridotites. To investigate the effect of subsolidus cooling on spinel Cr#, we applied the model of Voigt & von der Handt (2011) to our samples. Using the recorded mineral compositions and modes of a peridotite sample, the model calculates the equilibrium mineral compositions and modes at a given temperature, based upon a variety of temperature-dependent subsolidus reactions. In particular, the Voigt & von der Handt (2011) model incorporates Al–Cr exchange between orthopyroxene and spinel, Al–Cr exchange between orthopyroxene and clinopyroxene, and the Tschermak reaction, which produces spinel and Al-poor orthopyroxene at the expense of olivine and Al-rich orthopyroxene during cooling. We calculated equilibrium spinel Cr#s for Group I and Group II peridotites at temperatures between 700°C and 1300°C and found that no sample deviated from its recorded spinel Cr# by more than $\Delta Cr\# = 6$. As Group I and Group II peridotites differ by $\Delta Cr\# = 13\text{–}45$, subsolidus redistribution of Cr and Al cannot be responsible for the variation in spinel Cr# between Group I and Group II.

Subsolidus reactions also shift the absolute f_{O2} recorded by peridotites as a function of the P–T–t cooling path (e.g. Ballhaus, 1993; Woodland *et al.*, 1996),

although the magnitude of this effect is not well constrained. To test the effect of subsolidus cooling on f_{O2}, we used the Voigt & von der Handt (2011) model for Cr–Al redistribution, and added a reaction for Mg–Fe^{2+} exchange between olivine and spinel (Li *et al.*, 1995) to the model framework, as the Mg/Fe^{2+} ratio of these minerals affects fayalite and magnetite activities. Our modeling suggests that the f_{O2} values of equilibrium assemblages with the bulk composition of Group I and Group II peridotite samples, calculated between 700 °C and 1100 °C, vary by no more than 0·3 log units from the original recorded f_{O2} values for the samples, relative to QFM (above 1100 °C, the solver failed to converge for some samples). Our model does not incorporate ferric iron partitioning between phases, which is poorly constrained during subsolidus cooling. However, our results suggest that the difference in f_{O2}, which is of the order of two log units between Group I and Group II samples, is due to their chemical composition at the time of melt extraction and/or interaction and not to closed-system *P–T–t* subsolidus cooling paths.

Implications for the oxidation state of arc mantle

The stark contrast between the geochemical signatures recorded by Group I and Group II peridotites supports the hypothesis that oxidation at arcs is caused by interaction with arc-related melts and fluids (e.g. Kelley & Cottrell, 2009; Evans, 2012; Brounce *et al.*, 2015). Modeling of the Group I peridotites indicates that they underwent either low degrees of melt addition (<0·005% for Tonga samples) or disequilibrium melting, which requires no melt addition (Figs 9 and 10). These peridotites record low f_{O2}, around QFM – 0·2, which is consistent with mid-ocean ridge peridotites that have seen no influence from subduction processes. In marked contrast, the Group II peridotites are best modeled by higher percentages of melt addition (0·04–0·5%), and the modeling additionally suggests that the interacting melts were probably arc tholeiites. These peridotites record significantly higher f_{O2} (around QFM + 1·7), suggesting a causal relationship between elevated oxygen fugacity and interaction with arc melts or fluids.

Although the lack of age and stratigraphic constraints for the Tonga peridotites precludes conclusive determination of their tectonic history, we find it most likely that the distinct signatures in the Group I versus Group II peridotites are representative of processes occurring during and following subduction initiation. Brounce *et al.* (2015) showed that Mariana forearc basalts from the very earliest stages of subduction initiation are not significantly oxidized above MORB. They also showed that the oxidized signature in arc melts develops in the first 10 Myr after subduction initiation, in conjunction with an increase in subduction-related trace elements. We propose that the Tonga forearc peridotites tell the same story from the perspective of the residue, with Group I

peridotites representing the earliest stages of subduction initiation and Group II peridotites developing their oxidized signature as subduction matures.

Our petrogenetic model for the Tonga forearc peridotites, based on the subduction initiation models of Reagan *et al.* (2010, 2015), Stern *et al.* (2012), and Todd *et al.* (2012), is summarized in Fig. 14. Subduction begins at the interface between two oceanic plates—the younger, less dense Australian Plate and the older, denser Pacific Plate (Fig. 14a). The dense Pacific Plate founders as subduction initiates, and asthenospheric mantle upwells to fill the gap left by the sinking plate. This rapid upwelling results in large degrees of relatively dry decompression melting (Fig. 14b) that leave a highly refractory mantle residue. We interpret our Group I peridotites to be the extremely refractory mantle residue of this melting event, analogous to the residue of Mariana FAB (Brounce *et al.*, 2015).

As the slab founders further, it will reach a depth at which pressure-driven dehydration reactions release aqueous fluids from the slab into the overlying mantle. These fluids react with the ultra-refractory peridotite residue to produce boninites—wet melts interpreted to have formed via flux melting of ultra-refractory harzburgite (Fig. 14c). As the arc system matures, the forearc mantle freezes into lithosphere and corner flow becomes established in the mantle wedge, bringing in fertile mantle asthenosphere. As the slab continues to dehydrate, aqueous fluids result in flux melting of this fertile material, producing arc tholeiitic melts (Fig. 14d). We interpret our Group II peridotites to be the residue of this flux melting. As the arc system matures further, portions of this more fertile residue freeze into the lithosphere. Over time, extensive erosion at the trench–slab interface exposes the various melt products and residues of subduction initiation (Fig. 14e), from forearc basalts, boninites, and arc tholeiites to their variably depleted and variably subduction-influenced residues (Fig. 14f).

Our results show that the forearc mantle is heterogeneously oxidized, although the implications for the mantle wedge are less well constrained. The implication of our model is that asthenospheric mantle in the proto-subduction region is not oxidized prior to subduction initiation, and that mantle oxidation occurs as the arc mantle interacts with oxidized subduction-related melts and fluids. This suggests that the oxidized signature of arc lavas is inherited at the source (i.e. by flux melting of mantle by oxidized slab fluids), rather than developed later owing to differentiation or degassing. Additionally, if this melt–rock interaction is localized, then the majority of the mantle wedge may not be oxidized relative to mid-ocean ridge mantle. Determining the extent of oxidation of wedge material is difficult as xenoliths brought up in arc volcanoes are—by their nature—material produced by melt–rock interaction.

Our results indicate that mantle wedge material can additionally be exposed in the forearc and can be used to provide constraints on the nature of oxidation in the mantle wedge. The Tonga forearc is undergoing a large
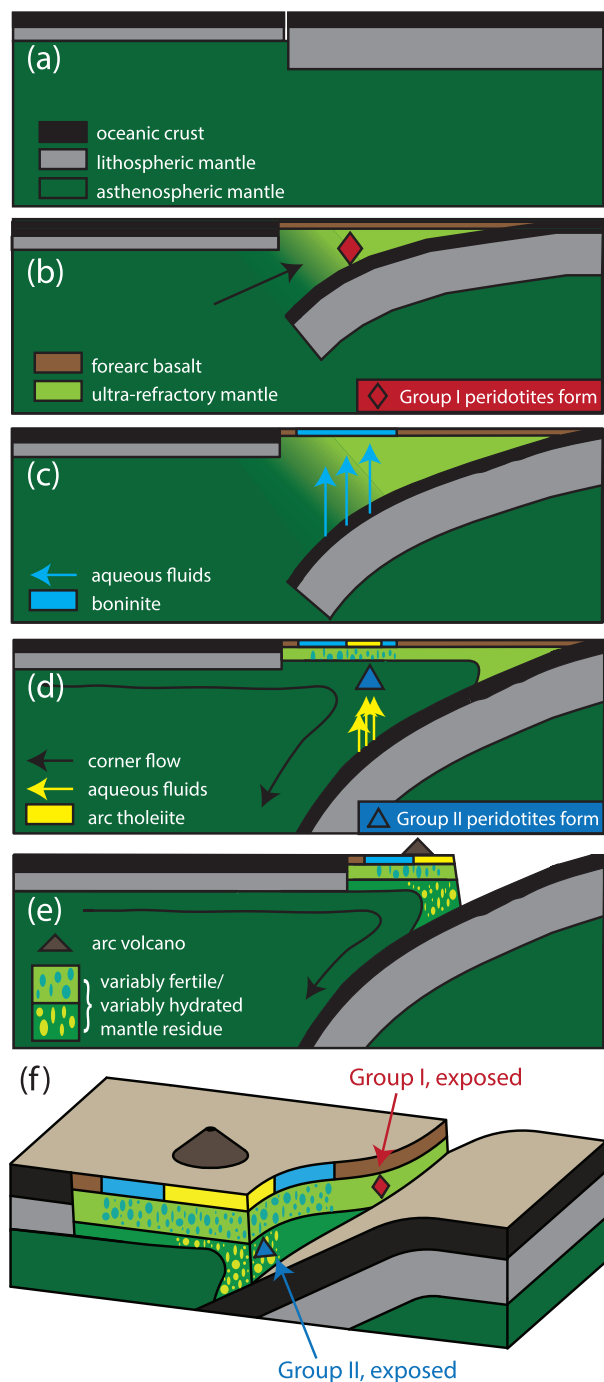
Fig. 14. Conceptual model for the petrogenesis of Tonga perido-tites. (a) Pre-subduction plate configuration. (b) As the denser plate founders, asthenospheric mantle upwells to fill in the gap left by the plate, leading to large degrees of decompression melting. Group I peridotites form as residues of this melting. (c) The plate sinks to a depth where hydrated phases break down, releasing fluids into the mantle wedge and triggering boninitic volcanism. (d) The arc system matures and corner flow is estab-lished. Fluids trigger flux melting in this more fertile astheno-sphere, leading to arc tholeiitic volcanism. Group II peridotites form as residues of this melting. (e, f) Erosion in the trench ex-poses the products of the various melting events associated with subduction initiation. Variable amounts of erosion from the trench interface can result in the exposure of lithologies with dif-ferent petrological histories, which may explain the heterogen-eity observed between dredges. It should be noted that *y*-axis and unit thicknesses are not to scale.

amount of tectonic erosion (e.g. Clift *et al.*, 1998; Wright *et al.*, 2000), and we interpret Group II peridotites to be flux-melted wedge material that froze into the litho-sphere before being exposed in the forearc by this ero-sion. Group II peridotites have evidently interacted with arc melts and fluids. If interaction with arc melts and flu-ids is localized within the wedge, the forearc would also have the potential to expose mantle wedge material that has not interacted with melts or fluids.

Our model predicts that samples of unreacted wedge material would be relatively fertile peridotites that have not undergone flux melting. These peridotites would not fit into either Group I or Group II, and would instead define a third group, consisting of lherzolites with low spinel Cr#, no evidence of LREE or fluid-mobile element enrichment, and f_{O_2} characteristic of the ridge peridotite array. The lone lherzolite so far identified (BMRG08-111-3-6) fits the spinel Cr# and f_{O_2} characteristics, although no site clearly representing this group has been observed. Regardless, more extensive sampling of fore-arc peridotites from global subduction zones could pro-vide crucial evidence of mantle wedge heterogeneity in addition to the observed forearc heterogeneity.

In summary, the heterogeneity of recorded oxygen fugacity between the Group I and Group II Tonga peri-dotites indicates that the forearc mantle is not perva-sively oxidized relative to normal, non-arc mantle. Group I peridotites, which are not oxidized above the mid-ocean ridge peridotite array, show little to no chemical evidence for having interacted with subduction-related melts or fluids. In contrast, Group II peridotites show chemical signatures associated with melt–rock interaction between residual mantle and arc melts, and are oxidized by ≥ 1 log unit above the mid-ocean ridge peridotite array. Additionally, the observa-tion that dredges comprising Group I samples are found both to the north and the south of the dredge containing Group II samples suggests that this difference in oxy-gen fugacity is not related to a simple change to a differ-ent tectonic or geochemical regime. Instead, the forearc mantle heterogeneously samples subduction-related processes. The correlation between elevated oxygen fu-gacity and chemical evidence for interaction with arc melts and fluids suggests that the sub-arc mantle is oxi-dized concurrently with addition of an oxidized slab component as subduction proceeds.

CONCLUSION

We show that Tonga forearc peridotites record hetero-geneous oxygen fugacity. The majority of the dredges analyzed in this study record f_{O_2} that is not elevated above the mid-ocean ridge peridotite array. These sam-ples are highly refractory, and we interpret them to be due to large degrees of near-fractional melting during the production of forearc basalts associated with sub-duction initiation. In addition, our recalculation of previ-ously reported oxygen fugacity data for peridotites leads us to conclude that some forearc locations

previously thought to have an oxidized subduction-related signature are, in fact, not oxidized above the mid-ocean ridge peridotite array.

In contrast, one Tonga Trench location (dredge BMRG08-106) records elevated f_{O2}. The lower spinel Cr#s and enriched light rare earth element concentrations suggest that this dredge has undergone a lower degree of fractional melting, as well as interaction with percolating hydrous melts and/or fluids. This most probably occurred during flux melting, as newly established corner flow brought fresh asthenospheric material into the mantle wedge. Modeling of REE patterns in these samples indicates that the melts and/or fluids involved in this flux melting are probably related to arc tholeiites associated with subduction initiation and later episodic volcanism. As these varieties of arc melts are generally oxidized, we conclude that the oxidized signature in these Tonga peridotites is probably imparted by oxidized melts and/or fluids during flux melting in a subduction setting.

SUPPLEMENTARY DATA

Supplementary data for this paper are available at *Journal of Petrology* online.

REFERENCES

Anders, E. & Grevesse, N. (1989). Abundances of the elements: Meteoritic and solar. *Geochimica et Cosmochimica Acta* **53**, 197–214.

Arculus, R. J., Ishizuka, O., Bogus, K. A., et al. (2015). A record of spontaneous subduction initiation in the Izu–Bonin–Mariana arc. *Nature Geoscience* **8**, 728–733.

Ballhaus, C. (1993). Redox states of lithospheric and asthenospheric upper mantle. *Contributions to Mineralogy and Petrology* **114**, 331–348.

Batanova, V., Suhr, G. & Sobolev, A. (1998). Origin of geochemical heterogeneity in the mantle peridotites from the Bay of Islands ophiolite, Newfoundland, Canada: ion probe study of clinopyroxenes. *Geochimica et Cosmochimica Acta* **62**, 853–866.

Bevis, M., Taylor, F. W., Schutz, B. E., et al. (1995). Geodetic observations of very rapid convergence and back-arc extension at the Tonga arc. *Nature* **374**, 249–251.

Bézos, A. & Humler, E. (2005). The $Fe^{3+}/\Sigma Fe$ ratios of MORB glasses and their implications for mantle melting. *Geochimica et Cosmochimica Acta* **69**, 711–725.

Birner, S. K., Warren, J. M., Cottrell, E. & Davis, F. A. (2016). Hydrothermal alteration of seafloor peridotites does not influence oxygen fugacity recorded by spinel oxybarometry. *Geology* G38113.1.

Bloomer, S. H. & Fisher, R. L. (1987). Petrology and geochemistry of igneous rocks from the Tonga trench: A non-accreting plate boundary. *Journal of Geology* **95**, 469–495.

Bloomer, S. H., Wright, D. J., MacLeod, C. J., et al. (1996). Geology of the Tonga forearc: A supra-subduction zone ophiolite. *EOS Transactions American Geophysical Union* OG32B-01.

Brey, G. P. & Köhler, T. (1990). Geothermobarometry in four-phase lherzolites II. New thermobarometers, and practical assessment of existing thermobarometers. *Journal of Petrology* **31**, 1353–1378.

Bodinier, J. L. & Godard, M. (2014). Orogenic, ophiolitic, and abyssal peridotites. In: Holland, H. & Turekian, K. (eds) *Treatise on Geochemistry*, 2nd edn. Elsevier, **3**, 103–167.

Borghini, G., Fumagalli, P. & Rampone, E. (2010). The stability of plagioclase in the upper mantle: Subsolidus experiments on fertile and depleted lherzolite. *Journal of Petrology* **51**, 229–254.

Brounce, M. N., Kelley, K. A. & Cottrell, E. (2014). Variations in Fe^{3+}/Fe of Mariana arc basalts and mantle wedge f_{O2}. *Journal of Petrology* **55**, 2513–2536.

Brounce, M., Kelley, K. A., Cottrell, E. & Reagan, M. K. (2015). Temporal evolution of mantle wedge oxygen fugacity during subduction initiation. *Geology* **43**, 775–778.

Brunelli, D., Seyler, M., Cipriani, A., Ottolini, L. & Bonatti, E. (2006). Discontinuous melt extraction and weak refertilization of mantle peridotites at the Vema lithospheric section (Mid-Atlantic Ridge). *Journal of Petrology* **47**, 745–771.

Bryndzia, L. T. & Wood, B. J. (1990). Oxygen thermobarometry of abyssal spinel peridotites: The redox state and C–O–H volatile composition of the Earth's sub-oceanic upper mantle. *American Journal of Science* **290**, 1093–1116.

Carmichael, I. S. E. (1991). The redox states of basic and silicic magmas: a reflection of their source regions? *Contributions to Mineralogy and Petrology* **106**, 129–141.

Clift, P. D., MacLeod, C. J., Tappin, D. R., Wright, D. J. & Bloomer, S. H. (1998). Tectonic controls on sedimentation in the Tonga Trench and Forearc, SW Pacific. *Geological Society of America Bulletin* **110**, 483–496.

Cottrell, E. & Kelley, K. A. (2011). The oxidation state of Fe in MORB glasses and the oxygen fugacity of the upper mantle. *Earth and Planetary Science Letters* **305**, 270–282.

Dare, S. A. S., Pearce, J. A., McDonald, I. & Styles, M. T. (2009). Tectonic discrimination of peridotites using f_{O2}–Cr# and Ga–Ti–FeIII systematics in chrome-spinel. *Chemical Geology* **261**, 199–216.

Davis, F. A., Cottrell, E., Birner, S. K., Warren, J. M. & Lopez, O. G. (2017). Revisiting the electron microprobe method of spinel–olivine–orthopyroxene oxybarometry applied to spinel peridotites. *American Mineralogist* **102**, 421–435.

Deschamps, F., Godard, M., Guillot, S. & Hattori, K. (2013). Geochemistry of subduction zone serpentinites: A review. *Lithos* **178**, 96–127.

Dick, H. J. B. (1989). Abyssal peridotites, very slow spreading ridges and ocean ridge magmatism. In: Saunders, A. D. & Norry, M. J. (eds) *Magmatism in the Ocean Basins. Geological Society, London, Special Publications* **42**, 71–105.

Dick, H. J. B. & Bullen, T. (1984). Chromian spinel as a petrogenetic indicator in abyssal and alpine-type peridotites and spatially associated lavas. *Contributions to Mineralogy and Petrology* **86**, 54–76.

Dygert, N. & Liang, Y. (2015). Temperatures and cooling rates recorded in REE in coexisting pyroxenes in ophiolitic and abyssal peridotites. *Earth and Planetary Science Letters* **420**, 151–161.

Elliott, T., Plank, T., Zindler, A., White, W. & Bourdon, B. (1997). Element transport from slab to volcanic front at the Mariana arc. *Journal of Geophysical Research* **102**, 14991–15019.

Evans, K. A. (2012). The redox budget of subduction zones. *Earth-Science Reviews* **113**, 11–32.

Falloon, T. J., Danyushevsky, L. V., Crawford, A. J., Meffre, S., Woodhead, J. D. & Bloomer, S. H. (2008). Boninites and adakites from the northern termination of the Tonga trench: Implications for adakite petrogenesis. *Journal of Petrology* **49**, 697–715.

Falloon, T. J., Meffre, S., Crawford, A. J., Hoernle, K., Hauff, F., Bloomer, S. H. & Wright, D. J. (2014). Cretaceous fore-arc basalts from the Tonga arc: Geochemistry and implications for the tectonic history of the SW Pacific. *Tectonophysics* **630**, 21–32.

Fisher, R. L. & Engel, C. G. (1969). Ultramafic and basaltic rocks dredged from the nearshore flank of the Tonga trench. *Geological Society of America Bulletin* **80**, 1373–1378.

Frost, B. R. (1991). Introduction to oxygen fugacity and its petrologic importance. In: Lindsley, D. L. (ed.) *Oxide Minerals. Mineralogical Society of America, Reviews in Mineralogy* **25**, 1–9.

Fryer, P., Ambos, E. L. & Hussong, D. M. (1985). Origin and emplacement of Mariana forearc seamounts. *Geology* **13**, 774–777.

Gaetani, G. A. & Grove, T. L. (1998). The influence of water on melting of mantle peridotite. *Contributions to Mineralogy and Petrology* **131**, 323–346.

Gaillard, F., Scaillet, B., Pichavant, M. & Iacono-Marziano, G. (2015). The redox geodynamics linking basalts and their mantle sources through space and time. *Chemical Geology* **418**, 217–233.

Gale, A., Dalton, C. A., Langmuir, C. H., Su, Y. & Schilling, J.-G. (2013). The mean composition of ocean ridge basalts. *Geochemistry, Geophysics, Geosystems* **14**, 489–518.

Godard, M., Lagabrielle, Y., Alard, O. & Harvey, J. (2008). Geochemistry of the highly depleted peridotites drilled at ODP Sites 1272 and 1274 (Fifteen-Twenty Fracture Zone, Mid-Atlantic Ridge): Implications for mantle dynamics beneath a slow spreading ridge. *Earth and Planetary Science Letters* **267**, 410–425.

Grocke, S. B., Cottrell, E., de Silva, S. & Kelley, K. A. (2016). The role of crustal and eruptive processes versus source variations in controlling the oxidation state of iron in Central Andean magmas. *Earth and Planetary Science Letters* **440**, 92–104.

Grove, T. L., Chatterjee, N., Parman, S. W. & Médard, E. (2006). The influence of H_2O on mantle wedge melting. *Earth and Planetary Science Letters* **249**, 74–89.

Hellebrand, E., Snow, J. E., Dick, H. J. & Hofmann, A. W. (2001). Coupled major and trace elements as indicators of the extent of melting in mid-ocean-ridge peridotites. *Nature* **410**, 677–681.

Herd, C. D. K. (2008). Basalts as probes of planetary interior redox state. In: MacPherson, G. J. (ed.) *Oxygen in the Solar System. Mineralogical Society of America and Geochemical Society, Reviews in Mineralogy and Geochemistry* **68**, 527–553.

Hirschmann, M. M., Ghiorso, M. S., Wasylenki, L. E., Asimow, P. D. & Stolper, E. M. (1998). Calculation of peridotite partial melting from thermodynamic models of minerals and melts. I. Review of methods and comparison with experiments. *Journal of Petrology* **39**, 1091–1115.

Ishizuka, O., Tani, K., Reagan, M. K., et al. (2011). The timescales of subduction initiation and subsequent evolution of an oceanic island arc. *Earth and Planetary Science Letters* **306**, 229–240.

Jagoutz, E., Palme, H., Baddenhausen, H., Blum, K., Cendales, M. & Dreibus, G. (1979). The abundances of major, minor and trace elements in the earth's mantle as derived from primitive ultramafic nodules. *Lunar and Planetary Science Conference Proceedings* **2**, 2031–2050.

Jochum, K. P., Stoll, B., Herwig, K., et al. (2006). MPI-DING reference glasses for *in situ* microanalysis: New reference values for element concentrations and isotope ratios. *Geochemistry, Geophysics, Geosystems* **7**, doi:10.1029/2005GC001060.

Johnson, K. T. M., Dick, H. J. B. & Shimizu, N. (1990). Melting in the oceanic upper mantle: An ion microprobe study of diopsides in abyssal peridotites. *Journal of Geophysical Research* **95**, 2661.

Kelemen, P., Shimizu, N. & Salters, V. (1995). Extraction of mid-ocean-ridge basalt from the upwelling mantle by focused flow of melt in dunite channels. *Nature* **375**, 747–753.

Kelley, K. A. & Cottrell, E. (2009). Water and the oxidation state of subduction zone magmas. *Science* **325**, 605–607.

Kelley, K. A., Plank, T., Ludden, J. & Staudigel, H. (2003). Composition of altered oceanic crust at ODP Sites 801 and 1149. *Geochemistry, Geophysics, Geosystems* **4**, doi: 10.1029/2002GC000435.

Lee, C.-T. A., Leeman, W. P., Canil, D. & Li, Z.-X. A. (2005). Similar V/Sc systematics in MORB and arc basalts: implications for the oxygen fugacities of their mantle source regions. *Journal of Petrology* **46**, 2313–2336.

Lee, C.-T. A., Luffi, P., Le Roux, V., Dasgupta, R., Albarède, F. & Leeman, W. P. (2010). The redox state of arc mantle using Zn/Fe systematics. *Nature* **468**, 681–685.

Li, J., Kornprobst, J., Vielzeuf, D. & Fabriès, J. (1995). An improved experimental calibration of the olivine–spinel geothermometer. *Chinese Journal of Geochemistry* **14**, 68–77.

Liang, Y. & Liu, B. (2016). Simple models for disequilibrium fractional melting and batch melting with application to REE fractionation in abyssal peridotites. *Geochimica et Cosmochimica Acta* **173**, 181–197.

Liang, Y., Sun, C. & Yao, L. (2013). A REE-in-two-pyroxene thermometer for mafic and ultramafic rocks. *Geochimica et Cosmochimica Acta* **102**, 246–260.

Lytle, M. L., Kelley, K. A., Hauri, E. H., Gill, J. B., Papia, D. & Arculus, R. J. (2012). Tracing mantle sources and Samoan influence in the northwestern Lau back-arc basin. *Geochemistry, Geophysics, Geosystems* **13**, 1–23.

Mallmann, G. & O'Neill, H. S. C. (2009). The crystal/melt partitioning of V during mantle melting as a function of oxygen fugacity compared with some other elements (Al, P, Ca, Sc, Ti, Cr, Fe, Ga, Y, Zr and Nb). *Journal of Petrology* **50**, 1765–1794.

Mattioli, G. S. & Wood, B. J. (1988). Magnetite activities across the $MgAl_2O_4$–Fe_3O_4 spinel join, with application to thermobarometric estimates of upper mantle oxygen fugacity. *Contributions to Mineralogy and Petrology* **98**, 148–162.

Meffre, S., Falloon, T. J., Crawford, T. J., Hoernle, K., Hauff, F., Duncan, R. A., Bloomer, S. H. & Wright, D. J. (2012). Basalts

erupted along the Tongan fore arc during subduction initiation: Evidence from geochronology of dredged rocks from the Tonga fore arc and trench. *Geochemistry, Geophysics, Geosystems* **13**, 1–17.

Montési, L. G. J. & Behn, M. D. (2007). Mantle flow and melting underneath oblique and ultraslow mid-ocean ridges. *Geophysical Research Letters* **34**, 1–5.

Morishita, T., Tani, K., Shukuno, H., Harigane, Y., Tamura, A., Kumagai, H. & Hellebrand, E. (2011). Diversity of melt conduits in the Izu–Bonin–Mariana forearc mantle: Implications for the earliest stage of arc magmatism. *Geology* **39**, 411–414.

Nell, J. & Wood, B. J. (1991). High-temperature electrical measurements and thermodynamic properties of Fe_3O_4–$FeCr_2O_4$–$MgCr_2O_4$–$FeAl_2O_4$ spinels. *American Mineralogist* **76**, 405–426.

Ohara, Y., Reagan, M. K., Bloomer, S. H., et al. (2008). Studies of the southern Izu–Bonin–Mariana (IBM) forearc using Shinkai 6500: watery glimpses of an *in situ* forearc ophiolite. *EOS Transactions American Geophysical Union* V33A–2194.

Palme, H. & O'Neill, H. (2014). Cosmochemical estimates of mantle composition. In: Holland, H. & Turekian, K. (eds) *Treatise on Geochemistry*, 2nd edn. Elsevier **3**, 1–39.

Parkinson, I. J. & Arculus, R. J. (1999). The redox state of subduction zones: insights from arc-peridotites. *Chemical Geology* **160**, 409–423.

Parkinson, I. J. & Pearce, J. A. (1998). Peridotites from the Izu–Bonin–Mariana forearc (ODP Leg 125): Evidence for mantle melting and melt–mantle interaction in a supra-subduction zone setting. *Journal of Petrology* **39**, 1577–1618.

Parkinson, I. J., Pearce, J. A., Thirlwall, M. F., Johnson, K. T. M. & Ingram, G. (1992). Trace element geochemistry of peridotites from the Izu–Bonin–Mariana Forearc, Leg 125. In: Dearmont, L. H., Mazzullo, E. K., Stewart, N. J. & Winkler, W. R. (eds) *Proceedings of the Ocean Drilling Program, Scientific Results, 125*. Ocean Drilling Program, pp. 487–506.

Parkinson, I. J., Arculus, R. J. & Eggins, S. M. (2003). Peridotite xenoliths from Grenada, Lesser Antilles Island Arc. *Contributions to Mineralogy and Petrology* **146**, 241–262.

Pearce, J. A. & Parkinson, I. J. (1993). Trace element models for mantle melting: application to volcanic arc petrogenesis. In: Prichard, H. M., Alabaster, T., Harris, N. B. W.& Neary, C. R. (eds) *Magmatic Processes and Plate Tectonics. Geological Society*, Special Publications **76**, 373–403.

Pearce, J. A., Barker, P. F., Edwards, S. J., Parkinson, I. J. & Leat, P. T. (2000). Geochemistry and tectonic significance of peridotites from the South Sandwich arc–basin system, South Atlantic. *Contributions to Mineralogy and Petrology* **139**, 36–53.

Plank, T. & Langmuir, C. H. (1993). Tracing trace elements from sediment input to volcanic output at subduction zones. *Nature* **362**, 739–742.

Reagan, M. K., Ishizuka, O., Stern, R. J., et al. (2010). Fore-arc basalts and subduction initiation in the Izu–Bonin–Mariana system. *Geochemistry, Geophysics, Geosystems* **11**, 1–17.

Reagan, M. K., Pearce, J. A., Petronotis, K., et al. (2015). Expedition 352 summary. In: *Proceedings of the International Ocean Discovery Program, 352*. International Ocean Discovery Program, http://publications.iodp.org/proceedings/352/352.PDF, 1–32.

Resing, J. A., Rubin, K. H., Embley, R. W., et al. (2011). Active submarine eruption of boninite in the northeastern Lau Basin. *Nature Geoscience* **4**, 799–806.

Ryan, W. B. F., Carbotte, S. M., Coplan, J. O., et al. (2009). Global Multi-Resolution Topography synthesis. *Geochemistry, Geophysics, Geosystems* **10**, 1–9.

Sack, R. O. & Ghiorso, M. S. (1991a). Chromian spinels as petrogenetic indicators: Thermodynamics and petrological applications. *American Mineralogist* **76**, 827–847.

Sack, R. O. & Ghiorso, M. S. (1991b). An internally consistent model for the thermodynamic properties of Fe–Mg-titanomagnetite–aluminate spinels. *Contributions to Mineralogy and Petrology* **106**, 474–505.

Seyler, M., Lorand, J. P., Toplis, M. J. & Godard, G. (2004). Asthenospheric metasomatism beneath the mid-ocean ridge: Evidence from depleted abyssal peridotites. *Geology* **32**, 301–304.

Seyler, M., Lorand, J. P., Dick, H. J. B. & Drouin, M. (2007). Pervasive melt percolation reactions in ultra-depleted refractory harzburgites at the Mid-Atlantic Ridge, 15°20'N: ODP Hole 1274A. *Contributions to Mineralogy and Petrology* **153**, 303–319.

Sharp, W. D. & Clague, D. A. (2006). 50-Ma initiation of Hawaiian–Emperor Bend records major change in Pacific plate motion. *Science* 1281–1284.

Shaw, C. S. J. & Dingwell, D. B. (2008). Experimental peridotite–melt reaction at one atmosphere: A textural and chemical study. *Contributions to Mineralogy and Petrology* **155**, 199–214.

Shaw, D. M. (1970). Trace element fractionation during anatexis. *Geochimica et Cosmochimica Acta* **34**, 237–243.

Stagno, V., Ojwang, D. O., McCammon, C. A. & Frost, D. J. (2013). The oxidation state of the mantle and the extraction of carbon from Earth's interior. *Nature* **493**, 84–88.

Stern, R. J., Reagan, M., Ishizuka, O., Ohara, Y. & Whattam, S. (2012). To understand subduction initiation, study forearc crust: To understand forearc crust, study ophiolites. *Lithosphere* **4**, 469–483.

Stormer, J. C. (1983). The effects of recalculation on estimates of temperature and oxygen fugacity from analyses of multicomponent iron–titanium oxides. *American Mineralogist* **68**, 586–594.

Syracuse, E. M., van Keken, P. E., Abers, G. A., Suetsugu, D., Bina, C., Inoue, T., Wiens, D. & Jellinek, M. (2010). The global range of subduction zone thermal models. *Physics of the Earth and Planetary Interiors* **183**, 73–90.

Tani, K., Shukuno, H., Hirahara, Y., Chang, Q., Kimura, J., Nichols, A. R., Ishii, T., Tatsumi, Y. & Dunkley, D. J. (2009). Evidence for silicic crust formation in an incipient stage of intra-oceanic subduction zone: discovery of deep crustal sections in Izu–Bonin forearc. *EOS Transactions American Geophysical Union*, T23A–1877.

Tatsumi, Y., Sakuyama, M., Fukuyama, H. & Kushiro, I. (1983). Generation of arc basalt magmas and thermal structure of the mantle wedge in subduction zones. *Journal of Geophysical Research* **88**, 5815.

Taylor, B., Zellmer, K., Martinez, F. & Goodliffe, A. (1996). Sea-floor spreading in the Lau back-arc basin. *Earth and Planetary Science Letters* **144**, 35–40.

Todd, E., Gill, J. B. & Pearce, J. A. (2012). A variably enriched mantle wedge and contrasting melt types during arc stages following subduction initiation in Fiji and Tonga, southwest Pacific. *Earth and Planetary Science Letters* **335–336**, 180–194.

Tollan, P. M. E., O'Neill, H. S. C., Hermann, J., Benedictus, A. & Arculus, R. J. (2015). Frozen melt–rock reaction in a peridotite xenolith from sub-arc mantle recorded by diffusion of trace elements and water in olivine. *Earth and Planetary Science Letters* **422**, 169–181.

Turner, S., Hawkesworth, C., Rogers, N., Bartlett, J., Worthington, T., Hergt, J., Pearce, J. A. & Smith, I. (1997). ^{238}U–^{230}Th disequilibria, magma petrogenesis, and flux rates beneath the depleted Tonga–Kermadec island arc. *Geochimica et Cosmochimica Acta* **61**, 4855–4884.

Van Orman, J. A., Grove, T. L. & Shimizu, N. (2002). Diffusive fractionation of trace elements during production and transport of melt in Earth's upper mantle. *Earth and Planetary Science Letters* **198**, 93–112.

Voigt, M. & von der Handt, A. (2011). Influence of subsolidus processes on the chromium number in spinel in ultramafic rocks. *Contributions to Mineralogy and Petrology* **162**, 675–689.

Warren, J. M. (2016). Global variations in abyssal peridotite compositions. *Lithos* **248–251**, 193–219.

Wood, B. J. (1990). An experimental test of the spinel peridotite oxygen barometer. *Journal of Geophysical Research* **95**, 15845–15851.

Wood, B. J. & Virgo, D. (1989). Upper mantle oxidation state: Ferric iron contents of lherzolite spinels by [57]Fe Mössbauer spectroscopy and resultant oxygen fugacities. *Geochimica et Cosmochimica Acta* **53**, 1277–1291.

Wood, B. J., Bryndzia, L. T. & Johnson, K. E. (1990). Mantle oxidation state and its relationship to tectonic environment and fluid speciation. *Science* **248**, 337–345.

Woodland, A. B., Kornprobst, J., McPherson, E., Bodinier, J.-L. & Menzies, M. A. (1996). Metasomatic interactions in the lithospheric mantle: petrologic evidence from the Lherz massif, French Pyrenees. *Chemical Geology* **134**, 83–112.

Wright, D. J., Bloomer, S. H., MacLeod, C. J., Taylor, B. & Goodlife, A. M. (2000). Bathymetry of the Tonga trench and forearc: a map series. *Marine Geophysical Researches* **21**, 489–511.